

JGR Space Physics

RESEARCH ARTICLE

10.1029/2020JA029087

Key Points:

- Magnetic field draping around Europa reduces ion surface flux onto the upstream hemisphere and enhances flux onto its downstream hemisphere
- Europa's upstream hemisphere receives the least amount of flux from energetic magnetospheric ions
- The flux pattern of sulfur ions is strongly correlated to observed surface variations in sulfuric acid concentration measured by Galileo

Correspondence to:

P. Addison,
paddison6@gatech.edu

Citation:

Addison, P., Liuzzo, L., Arnold, H., & Simon, S. (2021). Influence of Europa's time-varying electromagnetic environment on magnetospheric ion precipitation and surface weathering. *Journal of Geophysical Research: Space Physics*, 126, e2020JA029087. <https://doi.org/10.1029/2020JA029087>

Received 28 DEC 2020

Accepted 6 APR 2021

Influence of Europa's Time-Varying Electromagnetic Environment on Magnetospheric Ion Precipitation and Surface Weathering

Peter Addison¹ , Lucas Liuzzo² , Hannes Arnold¹ , and Sven Simon¹ 

¹School of Earth and Atmospheric Sciences, Georgia Institute of Technology, Atlanta, GA, USA, ²Space Sciences Laboratory, University of California, Berkeley, CA, USA

Abstract We combine the electromagnetic fields from a hybrid model with a particle-tracing code to calculate the time-varying spatial distribution of magnetospheric ion flux onto the surface of Jupiter's moon Europa. The electromagnetic fields at Europa are perturbed by the sub-alfvénic interaction of the moon's ionosphere and induced dipole with the magnetospheric plasma. These perturbations substantially modify magnetospheric ion trajectories at all energies. We calculate spatially resolved surface flux maps of thermal and energetic ions for various distances between Europa and the center of Jupiter's magnetospheric plasma sheet. The upstream ion distributions are constrained through in-situ particle data from the Galileo and Juno spacecraft. These maps are then combined to obtain the average distribution of magnetospheric ion surface flux over a full synodic rotation. Our results show that the draping and pileup of the magnetic field reduce ion flux onto Europa's trailing hemisphere by several orders of magnitude, while a significant number of the incident ions are deflected onto the leading hemisphere. Taking into account the deflection of energetic ions in the draped electromagnetic fields shifts the region of minimum energetic ion surface flux from Europa's wakeside equator to its ramside equator. This generates an “inverted bullseye” pattern of energetic ion flux centered at the trailing apex. Despite drastic changes to the morphology of the ion surface flux when the alfvénic plasma interaction is included, we still find a strong correlation between variations of sulfuric acid concentration observed across Europa's surface by Galileo and our modeled sulfur influx pattern.

1. Introduction

The magnetic field of Jupiter (radius $R_J = 71,492$ km) generates a magnetosphere that extends $\sim 50 R_J$ at the sun-facing side and hundreds of R_J at the sun-averted side (Joy et al., 2002). The magnetic dipole axis of Jupiter is inclined by 9.6° against its rotational axis, causing the magnetic field to “wobble” when viewed from a fixed point at the rotational equator. This wobble creates periodic variations in the magnetospheric field near Jupiter's Galilean satellites. Europa, the smallest of the Galilean satellites (radius $R_E = 1,560.8$ km), orbits its parent planet at a distance of $9.38 R_J$, well within the magnetosphere. Europa possesses a dilute exosphere (e.g., Hall et al., 1995; R. E. Johnson et al., 2009; Saur et al., 2011) and a salty subsurface ocean (e.g., Khurana et al., 1998; Kivelson et al., 2000; Zimmer et al., 2000), and is a focus of the Europa Clipper and JUICE missions set to launch in the next decade.

Europa's tenuous atmosphere, comprised primarily of molecular oxygen (O_2), was first sighted by Hall et al. (1995) using the Hubble Space Telescope (HST). Unlike the other Galilean satellites, Europa's atmosphere is only marginally collisional, and as such is often referred to as an exosphere (R. E. Johnson et al., 2009). The ejection of surface molecules by magnetospheric charged particle impacts (sputtering) is the main mechanism of atmospheric generation (Plainaki et al., 2012, 2018). Sputtered H_2O either refreezes to the surface, or is broken up into H_2 and O by particle irradiation (Cassidy et al., 2013; Plainaki et al., 2013). Hydrogen is light enough to quickly escape the moon's gravitational influence, but O recombines into O_2 , which remains bound and forms the exosphere. Based on HST observations, Saur et al. (2011) identified pronounced asymmetries in oxygen emission spectra, especially between Europa's leading (wakeside) and trailing (ramside) hemispheres. Neutral water plumes emanating from Europa's surface have also been detected using HST observations (Roth et al., 2014) and Galileo magnetometer and plasma data (Arnold et al., 2019; Jia et al., 2018).

The magnetosphere of Jupiter is home to a zoo of plasma species that interact with and shape the magnetic field in a number of complex ways. At its orbital position within the magnetosphere, Europa is exposed to two plasma populations: a thermal population (energy $E < 5$ keV), and an energetic population ($E > 5$ keV). The thermal plasma nearly corotates with Jupiter and is confined to a plasma sheet close to its magnetic equatorial plane (e.g., Bagenal & Delamere, 2011; Khurana, 1997). Empirical models show that this sheet decreases in density with distance northward and southward according to a Gaussian distribution (Bagenal & Delamere, 2011; Hill & Michel, 1976). At Europa's orbital distance, the plasma sheet rotates with a period approximately equal to Jupiter's rotational period (≈ 10 h), much faster than Europa orbits (≈ 80 h). Therefore, the (nearly corotating) thermal plasma continually overtakes Europa with a relative speed of ~ 100 km/s (e.g., Bagenal et al., 2015; Kivelson et al., 2004, 2009).

Europa moves along a near-circular (eccentricity 0.009) prograde orbit with an inclination against Jupiter's rotational equator of only 0.47° . Kivelson et al. (1999) showed that variation in the background field along Europa's orbit mainly occurs in the horizontal (perpendicular to Jupiter's magnetic axis) field components B_r (radial) and B_ϕ (azimuthal). This can be attributed to two main mechanisms. First, the quasi-dipolar field lines of Jupiter are stretched radially outward by plasma originating from Io, causing B_r to vary strongly as the magnetic equator moves north and south of Europa (Connerney et al., 1981; Khurana, 1997; Seufert et al., 2011). Above the magnetic equator, the field lines point radially outward ($B_r > 0$), whereas below the magnetic equator they point radially inward ($B_r < 0$). Second, as the field lines traverse the denser, slower plasma in the plasma sheet, the segment threading the sheet is slowed below corotation velocity. The result is an azimuthal "bulge" antiparallel to the plasma flow (Khurana & Kivelson, 1993; Vasyliunas, 1983). This "sweepback" generates a nonzero B_ϕ component, which is positive when Europa is south of the center of the plasma sheet and negative when north of the center. The time variation of B_r and B_ϕ at Europa's position induces currents in the moon's conducting subsurface ocean, which generate a secondary field outside the moon (Kivelson et al., 2000). This secondary field can be represented as a dipole centered at Europa, with its magnetic moment antiparallel to the direction of the inducing field. Thus, the dipole moment is located in Europa's equatorial plane (Saur et al., 2010). Using Galileo magnetometer data, Zimmer et al. (2000) constrained the phase lag between the inducing field and induced field to be approximately zero, and the magnitude of the induced dipole to be approximately that expected for a perfectly conducting sphere.

Particles in Europa's atmosphere are ionized by the impinging plasma (mainly by electron impacts, see Saur et al., 1998), and accelerated by the Lorentz force, slowing the ambient plasma and diverting it around the moon. The deceleration of the incident plasma powers a system of Alfvén wings, which extend from Europa's ionosphere to the polar ionosphere of Jupiter (Bonfond et al., 2017; Neubauer, 1980, 1998). Europa's induced field weakens the Alfvén wing currents and reduces the cross-section of the Alfvén wing flux tubes (Neubauer, 1999; Volwerk et al., 2007).

The energetic ($E > 5$ keV) ions and electrons present along Europa's orbit possess significant velocities parallel to the magnetic field. Their large field-aligned velocities allow these particles to leave the plasma sheet and travel to the polar atmosphere of Jupiter, where they are mirrored and become trapped in a bounce motion between the planet's magnetic poles. As such, these energetic particles continually traverse the orbit of Europa, and are therefore significant contributors to surface bombardment and sputtering (Breer et al., 2019; Cassidy et al., 2013; Paranicas et al., 2009). While the composition of the energetic ion population along Europa's orbit is well known (hydrogen, oxygen, and sulfur; e.g., Cooper et al., 2001; Ip et al., 1998), the distribution of their respective charge states remains a matter of debate (Clark et al., 2016, 2020; Mauk et al., 2020; Nénon & André, 2019). The number density of the energetic ions is several orders of magnitude below that of the thermal ions (Mauk et al., 2004), and as such their contributions to the plasma currents and field perturbations can be neglected (e.g., Blöcker et al., 2016). It is therefore feasible to treat them as test particles, that is, particles that do not modify their local electromagnetic environment (e.g., Breer et al., 2019; Cassidy et al., 2013; Poppe et al., 2018).

Pospieszalska and Johnson (1989) were the first to model energetic ion precipitation onto Europa, tracing 30 keV sulfur ions forward in time and mapping the locations where they impacted the moon's surface. Their model treated the electromagnetic fields near Europa as uniform and unaffected by plasma perturbations. Europa's induced field had not yet been discovered, and as such was not included in their model. The results of Pospieszalska and Johnson (1989) showed the highest levels of ion bombardment in a circular

pattern around Europa's trailing/ramside apex. Since energetic particle impacts break down surface materials via radiolysis (Paranicas et al., 2001), their findings provided an explanation for the UV absorption profile measured by the Voyager spacecraft, which showed minimum albedo in the trailing hemisphere (T. V. Johnson et al., 1983).

Expanding upon the model of Pospieszalska and Johnson (1989), Cassidy et al. (2013) calculated surface fluxes of hydrogen, oxygen, and sulfur ions. The authors considered particle energies across the entire range detected by the Galileo *Energetic Particles Detector* (~1 keV–10 MeV, see Mauk et al., 2004). Their model agreed with the findings of Pospieszalska and Johnson (1989), the incident energetic ion flux is greatest in Europa's trailing hemisphere, and decreases when moving in longitude toward the leading/wakeside hemisphere. This is consistent with the studies of Saur et al. (2011) and Plainaki et al. (2013), who found the greatest exospheric oxygen density in the trailing hemisphere. Additionally, Cassidy et al. (2013) found that at higher energies (>10 keV), the increased velocity of ions parallel to the magnetic field allows them to impart greater flux at higher latitudes than the thermal plasma. Similar to Pospieszalska and Johnson (1989), Cassidy et al. (2013) treated the fields around Europa as uniform, despite evidence from Paranicas et al. (2000) that pileup of magnetic field lines at the ramside partially protects it from charged particle bombardment. Furthermore, Cassidy et al. (2013) considered only a single set of averaged, ambient thermal plasma and magnetic field values, assuming the effects of variations in these quantities on surface bombardment to average out over a full synodic rotation. The influx patterns modeled by Cassidy et al. (2013) were used by Dalton et al. (2013) to correlate charged particle surface impacts with sulfuric acid (H₂SO₄) concentrations measured on Europa's surface by the Galileo spacecraft.

However, energetic ion dynamics near Europa show significant variability in response to changing upstream magnetospheric conditions, as demonstrated recently by Breer et al. (2019). These authors investigated the effects of field perturbations at Europa on energetic ion surface precipitation, while including both plasma currents and the induced dipole. They applied the AIKEF hybrid code (Arnold et al., 2019; Arnold, Liuzzo, & Simon, 2020; Müller et al., 2011) to calculate the field perturbations associated with Europa's thermal plasma interaction. For the same species studied by Cassidy et al. (2013), and over a similar range of energies (1 keV–5 MeV), Breer et al. (2019) modeled ion trajectories backwards in time and calculated the “accessibility” of Europa's surface to the energetic ion population. In their study, accessibility is defined as the percentage of incident magnetospheric ions that can reach a given location on Europa's surface (Liuzzo et al., 2019b). Three cases were analyzed by Breer et al. (2019): (i) uniform southward background magnetic field, with no induced field or perturbations from the moon's interaction with the ambient magnetospheric plasma included, (ii) Europa *north* of the center of the plasma sheet ($B_r > 0$, $B_\phi \approx 0$) with the induced field included but no plasma perturbations, and (iii) Europa north of the center of the plasma sheet with the induced field *and* plasma perturbations included. The effect of different atmospheric density profiles on the field perturbations and the resulting ion precipitation patterns were also tested, such as an asymmetric atmosphere and the addition of a neutral water plume (for details, see Arnold et al., 2019 and Arnold, Liuzzo, & Simon, 2020).

For case (i), Breer et al. (2019) found that ions with starting energies below 100 keV, whose dominant motion (when the fields are uniform) is $\mathbf{E} \times \mathbf{B}$ drift, preferentially precipitate onto Europa's trailing hemisphere, with near-zero precipitation occurring in the leading hemisphere. Ions in the MeV regime may possess velocities parallel to the magnetic field lines that are significantly larger than the (azimuthal) $\mathbf{E} \times \mathbf{B}$ drift. Therefore, these ions impinge upon the moon mainly from the north and south. Only near Europa's equator, where the field lines are approximately tangential to the surface (since no plasma perturbations were considered in this case), was precipitation reduced. Both of these results were consistent with the findings of Cassidy et al. (2013).

In their case (ii), Breer et al. (2019) included a positive radial component (B_r) to the background field to probe the effects of Europa's induced dipole. The superposition of the induced and background fields creates a protective “shell” around Europa, partially “bulging” the magnetic field lines around the moon (Khurana et al., 1998; Zimmer et al., 2000). Only near the geographic equator, where the total field is approximately tangential to the surface, was accessibility significantly reduced for ions with energies greater than 100 keV (Breer et al., 2019). Energetic ions traveling along the magnetic field gyrate into the moon at high latitudes, thereby becoming depleted before reaching the equator. In this way, they found that the induced dipole is

able to slightly enhance the protection of Europa's equatorial regions. Except for a brief window near the center of the plasma sheet, Europa always possesses an induced magnetic moment along the Europa-Jupiter line. Therefore, Breer et al. (2019) suggested that enhanced equatorial shielding due to the induced field persists throughout a full synodic rotation, and would *not* average out over geologic timescales.

Perturbations from the plasma interaction with Europa's ionosphere and induced dipole were shown by Breer et al. (2019) to have a more drastic effect on surface precipitation than the dipole alone. With these plasma interaction effects included, Breer et al. (2019) found that Europa's entire surface was partially shielded from energetic ion precipitation, with the maximum accessibility at any point reaching only $\sim 80\%$. This high of an accessibility was only obtained in localized regions for ions below 5 MeV. Multiple small inhomogeneities (on length scales below $0.1 R_E$) in ion accessibility were generated by asymmetric ionization processes in Europa's exosphere. Additionally, Breer et al. (2019) found that a "patch" of increased accessibility was generated at the Jupiter-averted (anti-Jovian) apex. They suggest that at this location the asymmetric draping of the magnetic field lines adds a field component perpendicular to the surface (causing ions with large field-aligned velocities to precipitate onto the moon). Pileup of the magnetic field lines due to the slowing of the thermal plasma was found to drastically protect the trailing hemisphere, consistent with observational evidence from Paranicas et al. (2000). Only for energies above 5 MeV did the precipitation patterns become qualitatively similar to those obtained for uniform fields. Recent studies at other Galilean moons, such as Ganymede (Fatemi et al., 2016; Plainaki et al., 2015; Poppe et al., 2018) and Callisto (Liuzzo et al., 2019a, 2019b), also found the effects of field perturbations to be critical in understanding the surface distribution of energetic charged particle flux. These results, along with those of Breer et al. (2019), underscore the importance of including a realistic model of the field perturbations in the calculation of surface precipitation by energetic particles.

However, Breer et al. (2019) did not study the time evolution of surface precipitation patterns as Jupiter's magnetospheric plasma sheet sweeps over Europa. In other words, the question of whether any single surface region is continuously shielded from ion irradiation over a full synodic rotation has not yet been addressed. Surface weathering develops over geologic timescales, that is, millions of synodic rotations. To develop a more comprehensive picture of energetic ion precipitation that can be used for the purpose of understanding surface weathering and atmospheric genesis at Europa, the integrated effects of a full synodic rotation must first be constrained. Additionally, Breer et al. (2019) explored precipitation *patterns*, but did not quantify actual particle fluxes.

To close these gaps, this study models energetic and thermal ion *flux* patterns across Europa's surface for three ion species (hydrogen, oxygen, and sulfur), integrated across the entire range of energies observed by the Galileo spacecraft, while applying the AIKEF hybrid code to include a comprehensive picture of the perturbed fields at different distances between Europa and the center of the Jovian plasma sheet. In this way, we intend to show how energetic ion flux onto Europa evolves over time, what the averaged surface flux pattern looks like for an entire synodic rotation, and whether any regions on the moon are continuously protected from ion irradiation. In Section 2, we describe the methodology and numerical inputs of our plasma and particle tracing model. In Section 3, we present surface irradiation maps for multiple distances between Europa and the center of the plasma sheet, as well as averaged maps of energetic ion surface flux across an *entire* synodic rotation. We then revisit the correlation between sulfur ion flux and surface sulfuric acid concentrations proposed by Dalton et al. (2013), now under the lens of Europa's perturbed fields. The possible implications of our modeled fluxes on surface sputtering and atmospheric genesis are then explored. Finally, in Sections 3.5 and 3.6, we constrain the robustness of our results against anisotropic pitch angle distributions and ion loss via charge exchange in Europa's exosphere. The study concludes with a brief summary of our major findings in Section 4.

2. Model Description

To calculate magnetospheric ion flux onto Europa's surface we import three-dimensional (3D) electromagnetic field datasets from the AIKEF hybrid model (e.g., Müller et al., 2011) into the established GENTOO particle tracing model (e.g., Liuzzo et al., 2019b). Sections 2.1 and 2.2 give a brief overview of the properties and input parameters of both models.

2.1. Hybrid Plasma Simulations

To determine the 3D electromagnetic field configurations near Europa we use the established hybrid code AIKEF (Müller et al., 2011), which treats ions as individual macroparticles and electrons as a massless, charge-neutralizing fluid. The kinetic (particle) treatment of ions allows the model to resolve important features of ion gyration, such as non-Maxwellian velocity distributions and the ionospheric Hall effect. Kivelson et al. (2004) showed that the Hall conductance of Europa's ionosphere is approximately one-third of the Pedersen conductance, and therefore the ionospheric Hall effect can generate discernible asymmetries in the electromagnetic fields. The AIKEF model has been extensively applied to Jupiter's moons Callisto (Liuzzo et al., 2015, 2016, 2017, 2018, 2019a, 2019b) and Europa (Arnold et al., 2019; Arnold, Liuzzo, & Simon, 2020; Arnold, Simon, & Liuzzo, 2020; Breer et al., 2019) in preceding studies. Arnold et al. (2019) found excellent quantitative agreement between the magnetic fields provided by AIKEF and in-situ data from the Galileo magnetometer taken during the E26 flyby of Europa. Even fine structures associated with a local water vapor plume source could be reproduced, thereby providing compelling evidence of AIKEF's capability to provide a quantitatively realistic picture of Europa's magnetospheric interaction. In earlier studies, the model also succeeded in reproducing magnetic field and plasma data from Galileo's Callisto flybys (Liuzzo et al., 2015, 2016, 2017). In this section, we provide a brief description of the input parameters. For technical details on the setup of the Europa AIKEF model, the reader is referred to our four preceding publications on that moon.

For our hybrid simulations, we use the EPhiO coordinate system, centered at Europa. The x -axis points in the direction of corotation, the y -axis points toward the center of Jupiter, and the z -axis completes the right-handed system, that is, it is aligned with Jupiter's rotation axis. The extent of the AIKEF simulation domain is $-10R_E \leq x \leq 20R_E$, $-10R_E \leq y \leq 10R_E$, and $-30R_E \leq z \leq 30R_E$. The AIKEF code utilizes a hierarchical grid that allows for higher resolution in the vicinity of the moon. Analogous to Arnold et al. (2019), we use three levels of resolution centered at the Europa: $0.02R_E$ for $|x|, |y|, |z| \leq 1.5R_E$, then $0.04R_E$ for $1.5R_E < |x|, |y|, |z| \leq 3R_E$, and $0.08R_E$ for $|x|, |y|, |z| > 3R_E$.

Thermal plasma is initiated at the upstream face of the domain ($x = -10R_E$), and the magnetic field throughout the domain is initially set to a uniform background vector B_0 . The upstream ion population is modeled as singly charged with a particle mass $m_{up} = 18.5$ amu, and a bulk velocity $u_0 = 100$ km/s in the $+x$ direction. The ion and electron temperatures are set to $k_B T = 100$ eV (Kivelson et al., 2004). As the magnetospheric plasma travels through the box, it encounters Europa, where it interacts with the moon's induced dipole moment and ionosphere. The simulation is run until the plasma has made at least one complete crossing of the domain; that is, until the field configuration reaches a quasi-stationary state.

In-situ measurements at Europa have constrained the variations in the ambient magnetospheric field components with distance to the plasma sheet. To describe the background magnetic field vector near Europa at different points in time during a full oscillation of the plasma sheet we adopt the analytical model of Schilling et al. (2007):

$$\mathbf{B}_0(t) = -84\text{nT}\sin(\Omega t)\hat{\mathbf{x}} - 210\text{nT}\cos(\Omega t)\hat{\mathbf{y}} - 410\text{nT}\hat{\mathbf{z}}, \quad (1)$$

where Ωt is the angle between the projection of Jupiter's magnetic moment axis onto Europa's orbital plane and the straight line connecting Europa to Jupiter (see Figure 1 of Neubauer, 1999). The quantities $\hat{\mathbf{x}}$, $\hat{\mathbf{y}}$, and $\hat{\mathbf{z}}$ are the unit basis vectors of the EPhiO system. This model is a fit to data from multiple Galileo crossings of Europa's orbit (Kivelson et al., 1999). Recent modeling of Jupiter's magnetic field based on data from the Juno spacecraft (Connerney et al., 2018, 2020) asserts that there may be a greater degree of north-south asymmetry in the magnetic field than was suggested by models from the Pioneer/Voyager era. However, the asymmetry identified by Connerney et al. (2018, 2020) is negligible within the close distances to the magnetic equator traversed by Europa over a synodic rotation. The far greater uncertainty in constraining the plasma interaction stems from the significant deviations between different models of the upstream plasma density (see discussion below). We therefore assume symmetry in the magnetic field about the magnetic equator as given by Equation 1.

The magnetic moment induced in Europa's subsurface ocean is given by (e.g., Arnold, Liuzzo, & Simon, 2020),

$$\mathcal{M}_{ind} = -\frac{2\pi R_E^3}{\mu_0}(B_{x,0}\hat{\mathbf{x}} + B_{y,0}\hat{\mathbf{y}}), \quad (2)$$

where $B_{x,0} = -84 \sin(\Omega t)$ and $B_{y,0} = -210 \cos(\Omega t)$. This model is consistent with the analysis of the induction signatures observed during Galileo's Europa flybys (Zimmer et al., 2000).

Along with the background field, the number density of the ambient magnetospheric plasma that interacts with Europa varies throughout a synodic rotation. We use the Gaussian density profile of Hill and Michel (1976),

$$n_p(h_{ps}) = n_{p,0} \exp\left(-\frac{h_{ps}^2}{H^2}\right), \quad (3)$$

where $n_p(h_{ps})$ is the ambient plasma number density at a given distance h_{ps} between Europa and the center of the plasma sheet, $n_{p,0}$ is the maximum number density at the center of the plasma sheet, and H is an empirically determined scale height. The quantities $n_{p,0}$ and H at Europa's orbit have been constrained by multiple authors using various sets of in-situ measurements, but no consensus has been reached on their values. The study of Bagenal and Delamere (2011) suggests values of $n_{p,0} \approx 50 \text{ cm}^{-3}$ and $H = 1.8 R_J$, respectively, based on data from the *Plasma Subsystem* (PLS) and *Plasma Wave Subsystem* (PWS) of the Voyager 1 spacecraft, and the PLS of the Galileo spacecraft. Roth et al. (2014) showed that values $n_{p,0} = 200 \text{ cm}^{-3}$ and $H = 0.9 R_J$ approximately reproduce the upstream densities observed during 8 of the 11 targeted flybys of Europa, as observed by the Galileo PWS (Kurth et al., 2001). For our model, we adopt the values of Roth et al. (2014). Applying these values to Equation 3, we find that the upstream density at Europa ranges from a maximum value of 200 cm^{-3} at the center of the plasma sheet to 40 cm^{-3} at Europa's maximum distance from the center of the plasma sheet. Using the values given by Bagenal and Delamere (2011), the upstream density would range between 50 and 37 cm^{-3} . Therefore, our density model (which uses the values of Roth et al., 2014) deviates by less than 10% far that of Bagenal and Delamere (2011) far from the center of the plasma sheet, but deviates by a factor of 4 at the center of the plasma sheet. At Europa's maximum distance from the center of the plasma sheet, we therefore expect our modeled surface fluxes to be almost identical to those that would be obtained using the density values of Bagenal and Delamere (2011).

We treat Europa's atmosphere as consisting entirely of molecular oxygen (e.g., Plainaki et al., 2013, 2018), and use the asymmetric number density profile of Arnold, Simon, and Liuzzo (2020) and Arnold, Liuzzo, and Simon (2020),

$$\begin{aligned} n_{n,L}(h) &= n_{n,0} \cdot \exp\left(-\frac{h}{h_0}\right), \quad 90^\circ < \alpha \leq 180^\circ \\ n_{n,T}(h, \alpha) &= n_{n,L}(h) \cdot (1 + A \cdot \cos(\alpha)), \quad \alpha \leq 90^\circ \end{aligned} \quad (4)$$

where $n_{n,L}(h)$ and $n_{n,T}(h)$ are the neutral atmospheric densities in the leading ($x > 0$) and trailing ($x < 0$) hemispheres, respectively. The quantity h is the height above Europa's surface, h_0 is the atmospheric scale height, $n_{n,0}$ is the number density of the neutral gas at the surface in the moon's wakeside hemisphere, and α is the angle between the negative x -axis and the radial unit vector connecting the center of Europa to a particular point. We use values of $5 \times 10^{13} \text{ cm}^{-3}$ and 100 km, respectively, for $n_{n,0}$ and h_0 , which Arnold et al. (2019) showed to be in good agreement with HST observations by Hall et al. (1995). The parameter A controls the degree of asymmetry between the two hemispheres. We set $A = 10$, in agreement with Arnold, Liuzzo, and Simon (2020) and Arnold, Simon, and Liuzzo (2020). We include only electron impact ionization in our model, as solar UV ionization has been shown to be weaker by an order of magnitude (Saur et al., 1998).

To model the time evolution of magnetospheric ion precipitation onto Europa, we examine three cases, representing three unique locations of Europa relative to the center of the Jovian plasma sheet: Europa located at the (1) *center* of the plasma sheet, (2) maximum distance h_{ps} *north* of the plasma sheet, and (3) maximum distance h_{ps} *south* of the plasma sheet. The relevant parameters for each case are given in Table 1.

Table 1
Simulation Parameters for the AIKEF and GENTOO Models

		Case (1)	Case (2)	Case (3)
Position relative to the plasma sheet		Center	Max. North	Max. South
AIKEF simulation parameters (Section 2.1)				
Ωt (°)	Magnetic latitudinal angle	90	0	180
h_{ps} (R_J)	Distance from the plasma sheet	0	0.98	-0.98
H (R_J)	Scale height	0.9	0.9	0.9
\mathbf{B}_0 (nT)	Background magnetic field	(-84, 0, -410)	(0, -210, -410)	(0, 210, -410)
\mathcal{M}_{ind} ($\frac{J}{nT}$)	Induced magnetic moment	($1.6 \cdot 10^{27}$, 0, 0)	($0, 4 \cdot 10^{27}$, 0)	($0, -4 \cdot 10^{27}$, 0)
\mathbf{u}_0 ($\frac{km}{s}$)	Plasma bulk velocity	(100, 0, 0)	(100, 0, 0)	(100, 0, 0)
$n_{p,0}$ (cm^{-3})	Thermal plasma density	200	40	40
$k_B T$ (eV)	Plasma temperature	100	100	100
$\mathbf{V}_{A,0}$ ($\frac{km}{s}$)	Alfvén velocity	(± 30 , 0, ± 147)	(0, ± 172 , ± 335)	(0, ∓ 172 , ∓ 335)
M_A^*	Alfvénic Mach number	0.67	0.33	0.33
β^{**}	Plasma beta	0.046	0.038	0.038
GENTOO simulation parameters (Section 2.2)				
n_O (cm^{-3})	Thermal oxygen number density	112	22	22
n_S (cm^{-3})	Thermal sulfur number density	60	12	12
n_H (cm^{-3})	Thermal hydrogen number density	28	6	6
-	Flyby data set for intensity spectra	E12	E26	E26

$$*M_A = \frac{|\mathbf{u}_0|}{|\mathbf{V}_{A,0}|}, \quad **\beta = \frac{2\mu_0 n_0 k_B T}{B_0^2}.$$

2.2. Particle Tracing

To calculate the trajectories of magnetospheric ions near Europa we utilize the particle-tracing code GENTOO (Breer et al., 2019; Liuzzo et al., 2019a, 2019b, 2020). In the GENTOO model, once an ion is initialized on the surface of Europa, it is traced *backwards* in time as it moves under the influence of the perturbed electromagnetic fields. The trajectories of energetic hydrogen (protons), oxygen, and sulfur ions with discrete starting energies in the range of ~ 1 keV–10 MeV are calculated, as they are the dominant energetic ion populations near Europa’s orbit (e.g., Cooper et al., 2001; Kim et al., 2020; Paranicas et al., 2000). In analogy to Breer et al. (2019), we do not consider relativistic mass growth of the particles, since the largest relativistic Lorentz factor for the chosen upstream distributions (that of 10 MeV hydrogen) deviates from the nonrelativistic value of 1 by only 1%.

In addition, the trajectories of protons, oxygen, and sulfur ions making up the thermal, corotating plasma population are calculated. For each particle species and energy, we establish a spherical starting grid on Europa’s surface, with latitude λ ranging from 90° at the north pole to -90° at the south pole, and longitude ϕ ranging clockwise (when viewed from the north) from 0° to 360° , with 0° located at the Jupiter-facing apex. The latitudinal resolution in position space, $\Delta\lambda = 2^\circ$, and the longitudinal resolution in position space $\Delta\phi = 4^\circ$. This yields $90 \times 90 = 8,100$ nodes located on a grid encompassing Europa’s surface. At each node, particles are launched at discrete angles against the local axis normal to Europa’s surface, defining a half-sphere in velocity space with a latitudinal resolution of $\Delta\theta_v = 3^\circ$ and a longitudinal resolution of $\Delta\phi_v = 3^\circ$. This yields $30 \times 120 = 3,600$ particles launched at each grid node. The number of particles in each GENTOO

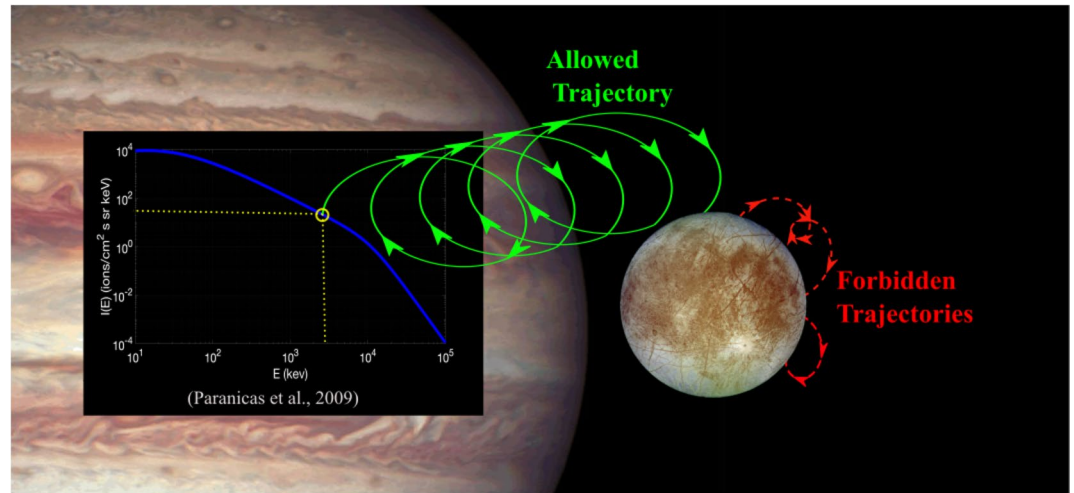


Figure 1. Illustration of how the GENTOO model calculates surface flux for energetic ions. Backtraced ions initialized on the surface either re-impact Europa (“Forbidden Trajectories”), or escape into the magnetosphere (“Allowed Trajectory”). The surface flux associated with “allowed” particles is calculated using Liouville’s theorem and empirical fits to Galileo EPD data, provided by Paranicas et al. (2002, 2009).

simulation is therefore $8,100 \times 3,600 \approx 29,000,000$. Each simulation traces particles of a *single* species and initial energy, thereby allowing analysis of the individual contribution of each species and energy to surface flux at a given location. The particles traced by GENTOO are “macroparticles,” that is, each of them represents a large number of actual ions, but has the same charge-to-mass ratio as the real particles.

Backtraced particles that re-encounter Europa’s surface (referred to as “Forbidden Trajectories”) are deleted, as these do not represent realistic trajectories: such a particle would have to pass *through* the solid body of Europa to reach its starting location on the surface. Alternatively, ions that never re-encounter Europa’s surface have “allowed trajectories.” An energetic particle that leaves Europa’s interaction region can theoretically travel to the Jovian polar ionosphere, bounce back, and re-encounter Europa. However, Paranicas et al. (2009) showed that the minimum time required for energetic ions to bounce back to Europa’s orbit is large enough that ions return too far downstream to re-interact with the moon. For example, a 1 MeV sulfur ion requires 485 s to travel along a magnetic field line from Europa to the Jovian polar ionosphere and back (Paranicas et al., 2009). By the time this ion returns, the “guiding” magnetic field line will have traveled at least $30 R_E$ downstream. Depending on the charge state, the gyroradius of a 1 MeV sulfur ion is no larger than $\approx 0.36 R_E$. Therefore, the returning particle will not re-enter Europa’s interaction region. As such, ions are deleted in our model once they leave Europa’s interaction region, consistent with the approach of Cassidy et al. (2013), Liuzzo et al. (2019b), and Breer et al. (2019).

Perturbations in the electromagnetic fields due to the thermal plasma interaction at Europa are limited to within $10 R_E$ of the moon, except for highly localized perturbations within the two Alfvénic flux tubes (e.g., Arnold, Liuzzo, & Simon, 2020). The gyroradii in the energy range considered (≈ 1 keV–10 MeV) vary between approximately $10^{-3} R_E$ and $1.4 R_E$. Particles are therefore considered “escaped” when at least one of their position coordinates (x, y, z) is outside the cube defined by $|x|, |y|, |z| \leq 15 R_E$, and their trajectories are designated as allowed. At this distance, it is impossible for an ion to gyrate back into the moon. We note that the cube defined by $|x|, |y|, |z| \leq 15 R_E$ is not entirely encompassed within the AIKEF domain (see Section 3.1). The electromagnetic fields are supplied by the AIKEF code while the particle is in the AIKEF domain. If a particle leaves the simulation domain, but has not yet met the condition to be designated “allowed,” the field at its position is set to the uniform background value used in the AIKEF model. An illustration of forbidden (red) versus allowed (green) trajectories is presented in Figure 1.

The thermal plasma is modeled as consisting of protons, singly charged oxygen ions, and doubly charged sulfur ions, consistent with Bagenal et al. (2015) and Kim et al. (2020). The charge states of heavy *energetic* ions at Europa are a matter of ongoing debate. Early data from the Ulysses spacecraft’s *Solar Wind Ion*

Composition Spectrometer showed that O^+ , O^{2+} , S^{2+} , and S^{3+} were the dominant ion species in the Jovian magnetosphere (Geiss et al., 1992). Clark et al. (2016) found that the charge states likely evolve with energy and radial distance to Jupiter, with higher charge states favored closer to the planet. Using a dispersion analysis of injection events measured by Galileo's EPD instrument, these authors suggested that the average charge states at Europa's approximate orbit are 1 ± 0.8 for oxygen and 3.9 ± 0.7 for sulfur. However, Clark et al. (2016) acknowledged that an injection event likely contains an admixture of ions at multiple charge states for each species. Nénon and André (2019) found evidence that the heavy ions near Europa have their charge attenuated by interactions with Europa's neutral gas torus. A recent study by Clark et al. (2020) inferred charge states using auroral megavolt electric potentials measured by the Jovian Energetic Particle Detector Instrument (JEDI) aboard the Juno spacecraft. They found that singly charged oxygen and doubly charged sulfur are the dominant energetic species in the outer magnetosphere. However, contrary to Nénon and André (2019), they hypothesized that the neutral gas torus along Europa's orbit strips electrons from the energetic heavy ions, redistributing them to *higher* charge states.

For our model of energetic ion precipitation, we track doubly charged oxygen (O^{2+}) and triply charged sulfur (S^{3+}), as these charge states are consistent with the range of values in Clark et al. (2016, 2020). Using these charge states also facilitates comparison between our results and those of Cassidy et al. (2013) and Breer et al. (2019) for Europa, Liuzzo et al. (2019b) for Callisto, and Poppe et al. (2018) for Ganymede. In addition, switching from an, for example, doubly charged oxygen ion to a singly charged oxygen ion of the same velocity only increases the ion gyroradius by a factor of 2, which is equivalent to increasing the energy of the doubly charged ion by a factor of 4. Reducing the charge of a sulfur ion from 3+ to 2+ would be equivalent to an even smaller change in energy. Therefore, differing charge states amount only to a slight shift (below an order of magnitude) of the energy at which ions are launched at the surface. Since our goal is to determine integrated flux maps for the entire energy range where significant ion fluxes were observed outside of Europa's interaction region, this slight energy shift does not have a significant effect on our conclusions.

Once a backtraced particle has met the condition for an "allowed" trajectory, its contribution to surface flux can be derived using Liouville's theorem and measurements of the ion distribution outside of Europa's interaction region. Liouville's theorem states that the phase space density f along a dynamical trajectory is conserved in the absence of collisions, that is, $f_s = f_e = f$, where f_s is the phase space density at the surface of Europa, and f_e is the phase space density at the point where GENTOO considers the ion to have escaped local interaction region. The application of Liouville's theorem at Europa is an approximation. Processes such as scattering by ion cyclotron waves (ICW) can modify f (e.g., Nénon et al., 2018), while interactions between energetic ions and whistler mode waves may cause localized phase space depletions (Shprits et al., 2018). Volwerk et al. (2001) and Desai et al. (2017) examined the properties of ICWs generated by exospheric ion pickup and observed near Europa during the Galileo E11 and E15 flybys. These authors identified ICWs in Europa's plasma wake within $\sim 3 R_E$ of the moon's surface. These waves may alter particle trajectories approaching Europa from downstream. However, the significance of wave-particle interactions to different ion populations at Europa's orbit is not well constrained through the limited available observations. In particular, there is no consensus on the growth times and saturation amplitudes of ICWs (Desai et al., 2017; Volwerk et al., 2001). Furthermore, ICWs emerge mainly from regions of strong temperature anisotropy (Šebek et al., 2016), the locations of which have not yet been constrained for Europa through observations or modeling. We therefore assume conservation of f as an approximation, analogous to the approach of Cassidy et al. (2013), Dalton et al. (2013), and Breer et al. (2019).

The differential number density dn of the plasma is defined as $dn = f d^3v$, where d^3v is the volume element in velocity space. In spherical coordinates, the volume element can be represented as

$$d^3v = v^2 dv \sin(\theta_v) d\theta_v d\phi_v, \quad (5)$$

where $v = \sqrt{\frac{2E}{m}}$ is the velocity of a particle of energy E and mass m . The angles θ_v and ϕ_v are the polar and azimuthal angles in velocity space, respectively, and $d\Omega_v$ is the solid angle element. The differential flux contribution onto the surface is given by

$$dJ = dn |\mathbf{v} \cdot \mathbf{e}_r|, \quad (6)$$

where \mathbf{e}_r is the local radial unit vector (normal to the surface at the location that the particle is initialized), and \mathbf{v} is the initial velocity vector of the backtraced particle at the surface. Combining Equations 5 and 6 yields an expression for the flux per macroparticle at the surface,

$$dJ = |\mathbf{v} \cdot \mathbf{e}_r| f v^2 dv d\Omega_v, \quad (7)$$

which can be rewritten in terms of energy,

$$dJ = |\mathbf{e}_v \cdot \mathbf{e}_r| f \frac{2E}{m^2} dE d\Omega_v, \quad (8)$$

where \mathbf{e}_v is the unit velocity vector of the particle when it impinges onto the surface. We initialize energetic ions with energies of 5, 10, 50, 100, 500, 1,000, 5,000, and 10,000 keV, covering the entire range of energies where significant energetic ion fluxes have been detected near Europa's orbit by the Galileo spacecraft (e.g., Mauk et al., 2004; Paranicas et al., 2002). The differential flux per energy,

$$\frac{dJ}{dE} = |\mathbf{e}_v \cdot \mathbf{e}_r| f \frac{2E}{m^2} d\Omega_v, \quad (9)$$

is calculated for each surface location and energy considered. The total number flux of a single species onto a certain location of Europa's surface is determined by integrating over the entire energy range studied,

$$J = \int \frac{dJ}{dE} dE, \quad (10)$$

with dE representing the difference between the discrete energy values listed above.

We assume that all backtraced ions that have "allowed" trajectories originate from the same ambient distribution, that is, we assume that this ambient distribution is uniform in position space (on the length scales of Europa's local interaction region). The phase space density of the thermal population outside of Europa's interaction region is approximated as a drifting Maxwell-Boltzmann distribution, centered around the bulk plasma velocity $\mathbf{u}_0 = u_0 \hat{\mathbf{x}}$:

$$f_{thermal}(\mathbf{v}) = n_0 \left(\frac{m}{2\pi k_B T} \right)^{\frac{3}{2}} \exp \left(\frac{-m(\mathbf{v} - \mathbf{u}_0)^2}{2k_B T} \right), \quad (11)$$

where n is the number density of the respective thermal ion species. The "heavy" thermal ions (O^+ and S^{2+}) have a temperature $k_B T = 100$ eV (Kivelson et al., 2009), while the thermal hydrogen population has a temperature of $k_B T = 20$ eV (Paterson et al., 1999). The ratios between the number densities of the three thermal species have been inferred by Bagenal et al. (2015). Using the total number density of the plasma from Equation 3, we can then constrain the densities of H^+ , O^+ , and S^{2+} at a given distance between Europa and the center of the plasma sheet. The resultant densities for all three cases are given in Table 1. In the GENTOO simulations, the thermal ions are initialized on Europa's surface with an energy that corresponds to the bulk plasma velocity \mathbf{u}_0 .

Unlike $f_{thermal}$, which accounts for the speed and direction of a particular particle, the phase space densities of the energetic ions must be constructed from in-situ energy spectra ($I(E)$) and an assumed pitch angle distribution (PAD). We use the intensity spectra (particles per [area \times time \times energy \times solid angle]) and fit

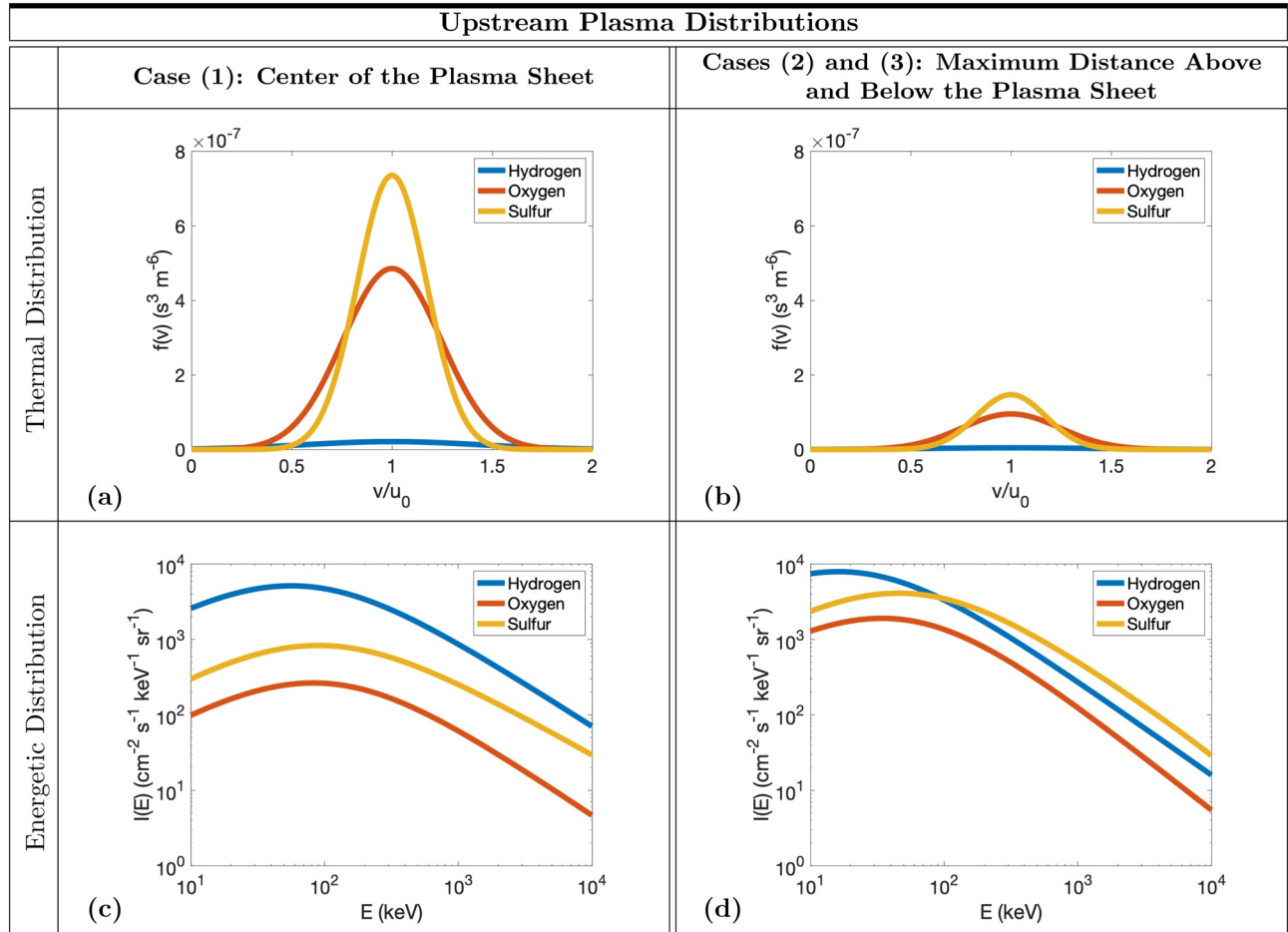


Figure 2. Upstream ion distributions used for the calculation of surface fluxes. Panels (a) and (b) show the thermal distributions f of each species for case (1) and cases (2)/(3), respectively. Panels (c) and (d) show the energetic ion intensities $I(E)$ by species used for case (1) and cases (2)/(3), respectively. The energetic distributions are empirical fits to Galileo EPD data from the E12 (case [1]) and E26 flybys (cases (2) and (3)), as shown in Paranicas et al. (2002).

equation of Paranicas et al. (2002, 2009), which are derived from Galileo EPD data (see Equation 2 and Table 1 of that study). To model the ambient energetic ion spectra when Europa is located at the center of the plasma sheet (case [1]), we employ an empirical fit to Galileo EPD data from the E12 flyby, which made its closest approach when Europa was at $h_{ps} \approx 0.1 R_J$. Similarly, for the maximum distance south of the plasma sheet (case (3)), we create an empirical fit to EPD data from the E26 flyby, which encountered Europa while it was close to its maximum distance south of the sheet ($h_{ps} \approx -1 R_J$).

Since the peer-reviewed literature does not provide ion energy spectra for Europa's maximum distance *north* of the plasma sheet, we assume the energetic ion distribution to be symmetric between the two sides of the plasma sheet and use the E26 distribution for case (2) as well. E12 and E26 data were taken from Figure 2 of Paranicas et al. (2002). Overall, the differences between the E12 and E26 spectra are rather subtle. Plots of the thermal distributions f and the intensity spectra $I(E)$ for all scenarios are given in Figure 2. This procedure is also illustrated in Figure 1.

To relate the total measured ion intensity $I(E)$ (which sums over all possible directions of the velocity vector at a given energy) to the ion intensity observable in a certain direction (defined by the angles θ_v and ϕ_v from Equation 6) we use the expression

$$\tilde{I}(E) = I(E) \times \frac{p(\alpha(\phi_v, \theta_v))}{\int_0^{2\pi} \int_0^\pi p(\alpha(\phi_v, \theta_v)) \sin \theta_v d\theta_v d\phi_v}, \quad (12)$$

where $\tilde{I}(E)$ is the angle-dependent intensity, the symbol α represents the pitch angle, and $p(\alpha(\phi_v, \theta_v))$ is a function that represents the variation in the intensity with the direction of \mathbf{v} . Typically this variation is axisymmetric around the direction of the background magnetic field, that is, it depends only on the pitch angle. The intensity spectra $\tilde{I}(E)$ given by Paranicas et al. (2002) assume the PAD to be uniform, that is, $p(\alpha(\phi_v, \theta_v))$ has a constant value. In this case, Equation 12 reduces to

$$\tilde{I}(E) = I(E) \times \frac{1}{4\pi}. \quad (13)$$

Mauk et al. (2004) found that the PAD of the energetic ions outside of Europa's interaction region is isotropic to within 2–5%, that is, the notion of isotropy would provide a reasonable representation of reality. However, recent evidence from Nénon and André (2019) showed that the energetic sulfur ions near Europa possess a “pancake” distribution, with a greater population of particles at pitch angles close to 90°. Such a distribution results from the loss of particles with large field-aligned velocities in Jupiter's atmosphere (forming the loss cone). Additionally, depending on their energy, the PAD of protons may change non-monotonically with pitch angle (Kollmann et al., 2016; Lagg et al., 2003).

Our calculations of surface flux in Sections 3.2–3.6 treat the PAD of the upstream energetic ions at Europa to be isotropic. To (approximately) model the effect of the pancake distribution of energetic sulfur ions observed by Nénon and André (2019), we have carried out an additional series of simulations for comparison, assuming the PAD for sulfur ions to be given by $p(\alpha(\phi_v, \theta_v)) \propto \sin(\alpha(\phi_v, \theta_v))$. This distribution is similar to the one found by Nénon and André (2019) for sulfur ions, and is consistent with the findings of Kollmann et al. (2016) for 130 keV protons with pitch angles not too close to 90°. Pospieszalska and Johnson (1989) applied a similar approach to study the role of an anisotropic PAD in sulfur ion precipitation onto Europa. Inserting this distribution into Equation 12 yields

$$\tilde{I}(E) = \frac{I(E)}{\pi^2} \sin \alpha(\phi_v, \theta_v). \quad (14)$$

The phase space density f can be related to the observed ion intensity in a given direction $\tilde{I}(E)$ through the expression

$$f_{\text{energetic}}(E) = \frac{m^2}{2E} \tilde{I}(E), \quad (15)$$

as shown by Kollmann et al. (2019).

Our magnetospheric flux maps in Sections 3.2–3.5 do not consider charge exchange reactions between incident ions and Europa's neutral exosphere. However, charge exchange reactions in Europa's exosphere may provide additional protection of Europa's surface from ion bombardment, especially from incident ions with energies below 100 keV. An energetic proton that captures an electron from an atmospheric O₂ particle will produce a new, slow moving O₂⁺ ion, as well as an energetic neutral atom (ENA) that will travel on a ballistic trajectory, unaffected by the electromagnetic field. The charge exchange cross sections begin to drop drastically above ~100 keV, and the effect of charge exchange reactions on surface precipitation weakens.

In analogy to Huybrighs et al. (2020), we implement the probabilistic charge exchange model of Birdsall (1991), where the probability of a charge exchange reaction P for an ion macroparticle at a certain position is given by

$$P = 1 - \exp(-n_n \sigma(E) v' |dt|). \quad (16)$$

The local neutral density n_n is the same profile used in AIKEF (see Equation 4), while $\sigma(E)$ is the energy-dependent charge exchange cross-section, v' is the velocity of the ion relative to the neutral gas (which is treated as a continuum), and $|dt|$ is the absolute value of the model time step. Europa's exosphere has a temperature of approximately 100 K (R. E. Johnson et al., 2009), and therefore the thermal velocity of the

neutral gas is about 200 m/s. Since the velocity of a 1 keV proton is already on the order of 10^5 m/s, we make the assumption that the exosphere is stationary (i.e., $v' = v$, where v is the velocity of the ion).

As an ion is traced backwards in time, the probability P of a charge exchange reaction is calculated at each time step. This value is then compared to a random number between 0 and 1 from a uniform distribution. If the probability P is greater than the random number, the ion is considered to have undergone a charge exchange reaction. A forward-traced counterpart ion that undergoes charge exchange would have to travel through *at least* as much neutral gas as its backtraced counterpart to reach the surface of the moon. Therefore, the elimination of a backtraced ion through a charge exchange reaction implies that the corresponding forward-traced ion must have an equal or greater chance of undergoing charge exchange before reaching the surface. Since charge exchange likely cannot neutralize a multiply charged oxygen or sulfur ion on the short length scales of Europa's exosphere (Nénon et al., 2018), we have carried out model runs including charge exchange reactions only for the magnetospheric proton population. Furthermore, cross-sections for charge exchange between neutral O_2 and O^{2+} and S^{3+} ions are not available in the peer-reviewed literature, so it is not currently possible to constrain the effects of charge exchange between Europa's exosphere and these species.

The inclusion of charge exchange reactions in this way *does not* violate Liouville's theorem. Ions (single-charged) that undergo charge exchange are immediately removed from the simulation, and are therefore never associated with any upstream distribution. An ion that never undergoes charge exchange follows a noncollisional trajectory, and the application of Liouville's theorem to that ion's trajectory is therefore valid.

Data on the charge exchange cross-section with neutral O_2 are available in the literature only for protons and O^+ , and only for energies up to 1 MeV (Basu et al., 1987; Lindsay & Stebbings, 2005). To determine the significance of this effect on our results, we have carried out simulations of protons with energies from 5 to 100 keV that includes charge exchange reactions for comparison.

We also note that a certain fraction of the ionospheric plasma generated near Europa will immediately hit the moon and contribute to surface flux. Ip et al. (1998) suggested that this "self-sputtering" by newly generated ionospheric ions could increase the production of exospheric neutrals by a factor of 10. However, the velocities of ionospheric ions near Europa are no more than 1% of the corotation velocity, as shown by Arnold, Liuzzo, and Simon (2020) and consistent with our AIKEF results. Such low energy ions have a negligible sputtering yield (Famá et al., 2008; R. V. Johnson et al., 2009) compared to the energetic ions. In addition, Ip et al. (1998) found that the factor of 10 enhancement in neutral gas production led to an overestimate of the exospheric column density compared to HST measurements (Hall et al., 1995). Therefore, in analogy to Cassidy et al. (2013) and Breer et al. (2019), we do not consider the contribution of slow ionospheric ions in our calculation of surface fluxes.

3. Results and Discussion

In Section 3.1, we present the results of our hybrid simulations, and discuss the important features of Europa's local electromagnetic environment. We then present integrated surface flux maps for different distances between Europa and the center of the plasma sheet in Sections 3.2 and 3.3. Total flux maps integrated over an entire synodic rotation are presented in Section 3.4. The effect of charge exchange reactions between energetic protons and Europa's atmosphere on surface flux is discussed in Section 3.6, while the effect of a nonisotropic PAD is examined in Section 3.5.

3.1. Structure of Europa's Electromagnetic Environment

Figure 3 displays the results of the hybrid simulations for cases (1)–(3). The inclusion of a horizontal background field component ($B_{x,0}$ in case (1) or $B_{y,0}$ in cases (2) and (3)) rotates the Alfvén wing characteristics $\mathbf{u}_0 \pm \mathbf{V}_{A,0}$ (where $\mathbf{V}_{A,0}$ is the Alfvén velocity in the undisturbed upstream flow, see, e.g., Neubauer, 1980), and breaks the symmetry of the interaction with respect to the xz (case (1)) or xy (cases (2) and (3)) plane of the EPhiO system. In case (1), the Alfvén characteristics are still contained in the xz plane, but are rotated around the y -axis by the angle $\theta_{\text{rot},y} = \arctan(B_{x,0}/B_{z,0})$. The Alfvén characteristics in cases (2) and (3)

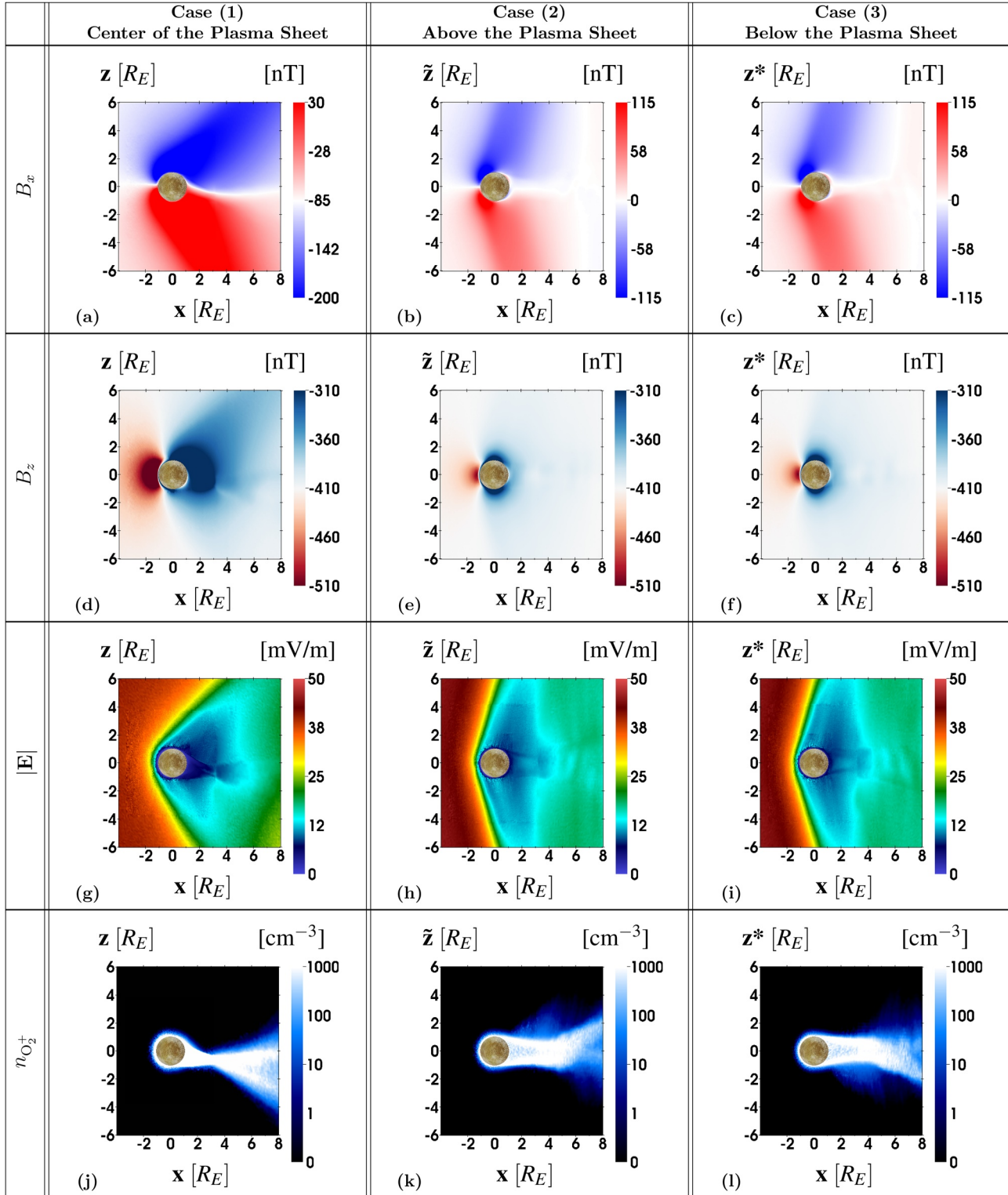


Figure 3. Hybrid simulation results for Europa at the center of the plasma sheet (case [1]), at maximum distance north of the plasma sheet (case [2]), and at maximum distance south of the plasma sheet (case [3]). Each column contains the result of a single case, while the rows show B_x (panels (a–c)), B_z (panels (d–f)), the magnitude of the electric field $|\mathbf{E}|$ (panels (g–i)), and the number density of O_2^+ pickup ions (panels (j–l)). Results for cases (2) and (3) are plotted in the planes (“ $x\tilde{z}$ ” and “ xz^* ,” respectively) that contain the center of Europa and the Alfvén characteristics $\mathbf{u}_0 \pm \mathbf{V}_{A,0}$, that is, they are rotated around the x -axis by

$$\theta_{rot,x} = \arctan\left(\frac{B_{y,0}}{B_{z,0}}\right).$$

are rotated around the x -axis by the angle $\theta_{\text{rot},x} = \arctan(B_{y,0}/B_{z,0})$, and are therefore no longer contained in the xz plane. Specifically, the Alfvén characteristics of case (2) are rotated counterclockwise around the x -axis when viewed from upstream, with the northern wing inclined toward Jupiter. For case (3), the characteristics are rotated clockwise, and the *southern* wing is inclined toward Jupiter. Therefore, for a better picture of the important physics, we display select quantities for cases (2) and (3) in Figure 3 in a rotated plane through the center of Europa ($x\tilde{z}$ and xz^* , respectively) that contains the Alfvén wing characteristics and the upstream flow velocity \mathbf{u}_0 . For a more comprehensive study of Europa's thermal plasma interaction under similar upstream conditions, the reader is referred to our preceding publications (Arnold et al., 2019; Arnold, Liuzzo, & Simon, 2020; Arnold, Simon, & Liuzzo, 2020).

The different orientations and strengths of the background field result in different induced dipole moments \mathcal{M}_{ind} from Europa's subsurface ocean, given in Table 1. The induced dipole moment in case (1) is oriented parallel to the upstream flow direction, while the dipole moments in cases (2) and (3) are oriented toward and away from Jupiter, respectively. The weaker inducing field component in case (1) means that the induced dipole field is 60% weaker at the center of the plasma sheet than at the maximum northern and southern distances (cases [2] and [3]).

The perturbations in the electromagnetic field near Europa are a result of the interaction of the upstream plasma with the moon's ionosphere and the induced dipole field. Notable in the B_x component of all three cases (Figures 3a–3c) is strong draping of the magnetic field around the moon's upstream apex. The interaction also generates a system of Alfvén wings, which carry perturbations in the field components and plasma flow far away from Europa's local interaction region (Neubauer, 1980, 1998), and ultimately give rise to the moon's auroral footprints in Jupiter's polar atmosphere (e.g., Bonfond et al., 2017). Since the inclination of the Alfvén wings against the background magnetic field \mathbf{B}_0 is given by the inverse tangent of the Alfvén Mach number M_A (see Table 1), the Alfvén wings are tilted closer to the flow ($+x$) axis in case (1) than in cases (2) and (3). Since the Alfvén characteristics in case (1) are rotated around the y -axis, the northern wing is inclined closer to the flow (45° from the z -axis) than the southern wing (22° from the z -axis). In cases (2) and (3), both the northern and southern wings are inclined 19° against the z -axis. The higher density of the upstream plasma $n_{p,0}$ in case (1) generates stronger perturbations in B_x compared to cases (2) and (3).

The strong induced dipole in cases (2) and (3) produces a noticeable reduction in the cross-sections of the Alfvén wing tubes (Figures 3b and 3c). This can be seen when comparing the widths of the Alfvén flux tubes in case (1), where the induced dipole is weak, to those in cases (2) and (3), where the induced dipole is 2.5 times stronger. These results are in qualitative agreement with theoretical predictions by Neubauer (1999) and analysis of Galileo magnetometer data from the Europa flybys by Volwerk et al. (2007). The results of cases (2) and (3) also reveal the formation of two highly localized ($<0.5R_E$ from the surface) regions in the leading hemisphere ($x > 0$) where the induced dipole field causes a reversal in the sign of the B_x perturbations. This can be seen in Figures 3b and 3c as a small positive perturbation (red region) adjacent to a larger region of negative B_x (blue) caused by the field line draping in the north ($z > 0$), and as a small negative perturbation (blue region) adjacent to a larger region of positive, draped B_x (red) in the south ($z < 0$). Hence, in this small wakeside region, the field lines are still close in shape to a “pure” induced dipole field, nearly unaffected by plasma currents. A similar wakeside region where the induced dipole field is still discernible despite the plasma perturbations has also been seen in Galileo magnetic field data from the C10 flyby of Callisto by Liuzzo et al. (2016), who labeled it the “quasi-dipolar core region.” The presence of this region in the wake is important for induction measurements, which can be used to constrain properties of Europa's subsurface ocean (e.g., Zimmer et al., 2000). However, in contrast to Callisto, where the inducing field can comprise $\sim 90\%$ of the total background field, the inducing field at Europa can only reach about 45% of the background field, and only at large distances to the plasma sheet (as in cases [2] and [3]). The quasi-dipolar core region in case (1) is not discernible in our plot (Figure 3a), as in this case, the inducing field is only $\sim 20\%$ of the background field, and the shrouding of the induced field by plasma currents is stronger due to the higher upstream density. The field configuration near Europa in case (1) is also qualitatively different from cases (2) and (3), as the induced dipole moment is *aligned* with the upstream flow direction and not perpendicular to it.

The north-south component B_z of the magnetic field is shown in Figures 3d–3f. A strong enhancement in the magnitude of B_z can be seen near the trailing apex due to the pileup of the field lines in the decelerated

upstream plasma. Downstream of the pileup region the field is reduced, as the draped field lines are diverted around the moon's ionosphere and induced dipole. Both the upstream enhancement and the downstream depletion in B_z are strongest at the center of the Jovian plasma sheet (Figure 3d), where the enhanced ram pressure of the incident flow allows for greater plasma-ionosphere interaction and field pileup.

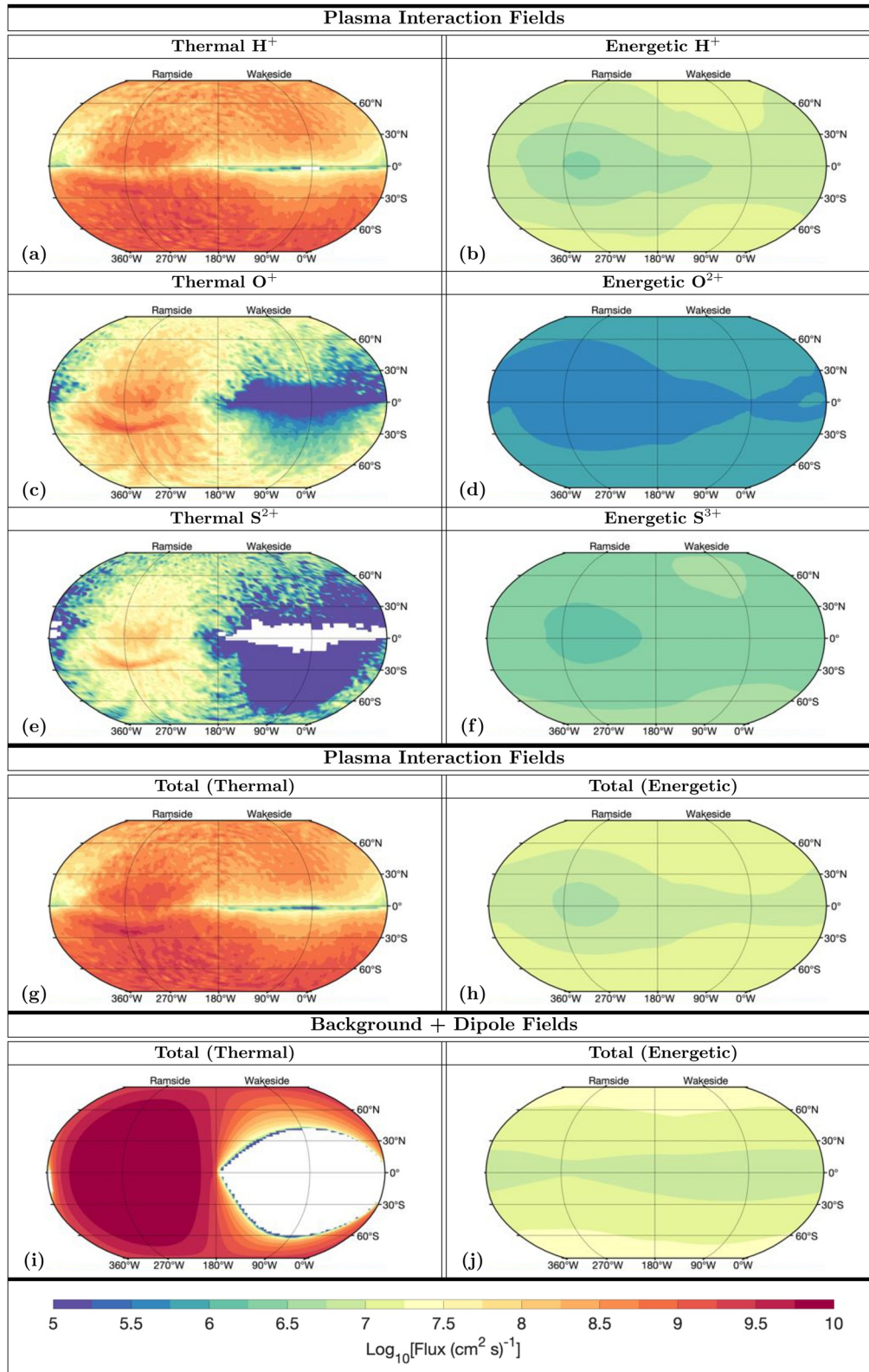
Similar to the findings of Arnold, Liuzzo, and Simon (2020) for Europa and Liuzzo et al. (2019b) for Callisto, the reduction in the magnitude of B_z downstream of the pileup region is most prominent in the regions where the background field is nearly perpendicular to the surface. This can be seen near $\tilde{z} = \pm 1R_E$ in Figure 3e and near $z^* = \pm 1R_E$ in Figure 3f. The negative background $B_{x,0}$ component in case (1) rotates the depletion in field strength clockwise around the y -axis, and the asymmetrically draped field lines have a greater component normal to the surface in the southern hemisphere than in the northern hemisphere. A similar asymmetry is not seen in case (2) or (3), where the background field is perpendicular to the x -axis.

The magnitude of the electric field is reduced downstream of Europa in all three cases (Figures 3g–3i). In a spherical shell surrounding Europa (within $\sim 0.5 R_E$ from the surface), newly ionized, slow-moving ionospheric particles dominate the overall plasma density (Figures 3j–3l), leading to a reduction in the bulk velocity. The convective electric field $\mathbf{E} = -\mathbf{u} \times \mathbf{B}$ is therefore reduced by a factor of ~ 50 within this shell, compared to the upstream electric field. At larger distances to Europa, the Alfvén wings divert plasma out of their geometric shadow, leading to a decrease in bulk plasma velocity downstream. Directly downstream of the moon, the slow-moving pickup ions form a tail with a width of $\sim 2 R_E$ perpendicular to the x -axis (Figures 3j–3l), where their density is still significant enough to reduce the bulk velocity and convective electric field. The result is a clearly discernible imprint of the pickup tail on the electric field, which extends beyond $x \approx 6 R_E$. The pickup tail in all three cases starts to fray out approximately $5 R_E$ downstream as it begins to fill the region of low plasma pressure between the two Alfvén wings, an effect also seen at Europa by Arnold, Simon, and Liuzzo (2020) and at Titan by Simon et al. (2006). The electric field gradually re-builds in strength with increasing x as the pickup ions are accelerated and as the thermal upstream plasma flow re-fills Europa's wake.

3.2. Ion Flux Onto Europa at the Center of the Plasma Sheet

Figure 4 displays the number flux of magnetospheric ions onto Europa while the moon is located near the center of the Jovian plasma sheet. Figures 4a–4h show the flux for the case of perturbed electromagnetic fields that include the Jovian background field, the European-induced dipole, and currents generated by the moon's interaction with the upstream plasma. The left column (Figures 4a, 4c, and 4e) shows the number flux by species onto the surface from the upstream thermal plasma (H^+ , O^+ , and S^{2+} , respectively). The right column (Figures 4b, 4d, and 4f) shows number flux by species onto the surface by the energetic ions (H^+ , O^{2+} , and S^{3+} , respectively), integrated over the energy range from 5 keV to 10 MeV. The total number flux across all species of the thermal plasma is given in Figure 4g, while the total flux of all energetic ion species is given in Figure 4h. To provide a “baseline” for the interpretation of these results, Figures 4i and 4j show total number flux across all species for an electromagnetic field configuration that does *not* include the plasma interaction, but only the background Jovian field and the induced dipole. We emphasize that this “baseline” setup is *not* the same as studied by Cassidy et al. (2013): those authors considered only the Jovian background field, but *not* the induced dipole. All quantities in Figure 4 are plotted left to right in the direction of decreasing West Longitude. The trailing apex (ramside) is located at $270^\circ W$, the leading apex (wakeside) is located at $90^\circ W$, and the Jupiter-facing and Jupiter-averted apices are located at $360/0^\circ W$ and $180^\circ W$, respectively.

Most apparent in the surface flux of the thermal plasma (Figures 4a, 4c, 4e, and 4g) is an enhancement by as much as eight orders of magnitude onto the trailing hemisphere (centered at $270^\circ W$) compared to the leading hemisphere (centered at $90^\circ W$). At thermal ion energies, the gyroradii are less than $0.1 R_E$ (specifically, $r_g(H^+) = 0.0015 R_E$, $r_g(O^+) = 0.025 R_E$, and $r_g(S^{2+}) = 0.025 R_E$), and it is impossible for them to impact the leading hemisphere by gyrating around the moon. When only the background Jovian magnetic field and the induced dipole are considered (Figure 4i), the upstream thermal plasma impinges almost exclusively onto Europa's trailing hemisphere. In this “baseline” configuration, the trailing hemisphere apex receives as much as $10^{10} \text{ cm}^{-2} \text{ s}^{-1}$ of flux. The flux onto the trailing hemisphere decreases with distance from the apex, forming a “bulls-eye” pattern. This is a result of the fact that the upstream plasma, moving along the



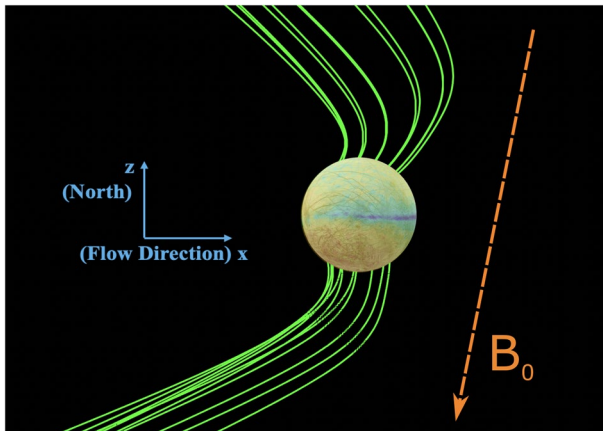


Figure 5. Thermal hydrogen trajectories (green) for case (1), as viewed in the direction of the positive y -axis. Jupiter would be located behind Europa in this view. The particles shown were initiated normal to Europa's surface in 30° longitudinal increments at 60° north and 60° south latitude and traced backwards in time. The map of thermal hydrogen flux for case (1) is superimposed on Europa's surface. The orientation of the Jovian background field is shown in orange.

x -axis, can directly impinge onto the moon's trailing hemisphere. Since the flux is dependent upon the angle relative to the surface at which an ion impacts, it decreases as the angle between the surface and the x -axis grows. The leading hemisphere between 30° north and 60° south latitude receives nearly zero flux (white region centered at 90° W in Figure 4i). This flux distribution is similar to that found by Cassidy et al. (2013) and Dalton et al. (2013), who treated the magnetic field as uniform and southward. The similarity of their results, which do not include the influence of Europa's induced dipole, to our results in Figure 4i indicates that at the center of the Jovian plasma sheet the induced dipole does not play a significant role in shielding the surface from thermal ion precipitation. This makes physical sense, as the induced dipole is at its weakest when Europa is located near the center of the sheet.

However, when the influence of the thermal plasma interaction is included (Figures 4a, 4c, 4e, and 4g), the thermal flux pattern changes significantly. While the ramside still receives the greatest amount of thermal ion flux (Figure 4g), it is reduced by over an order of magnitude compared to the case of only the Jovian background field and the induced dipole (Figure 4i). The pileup and draping of the magnetic field lines deflect upstream thermal ions around the moon, partially protecting the ramside apex and redistributing the flux across the surface. Most notably, when the plasma interaction is considered, the leading apex receives a

significant amount of thermal ion irradiation, while this region is almost completely protected without plasma currents. No region on Europa's surface receives less than $10^0 \text{ cm}^{-2} \text{ s}^{-1}$ from the upstream thermal plasma when perturbations due to the plasma interaction are included (Figure 4g). This is possible due to the draping of the magnetic field lines, as shown in Figures 3a and 3d.

To illustrate the mechanism responsible for this wakeside irradiation, Figure 5 shows trajectories (in green) of thermal hydrogen ions which impact normal to the surface in 30° longitudinal increments at 60° north and 60° south latitudes. In the northern hemisphere, thermal ions that impinge upon Europa's interaction region with highly inclined velocities against the x -axis intersect the draped field lines near the moon, obtain a velocity *against* the corotational flow direction (i.e., in the $-x$ direction), and impact the moon's wakeside surface. The particles that impact the southern hemisphere in Figure 5 intersect the draped field lines near Europa at shallower angles against the x -axis, and are therefore confined to impacting near the south pole. In this way, the draped magnetic field lines allow upstream thermal particles to access every location on Europa's surface, including the leading hemisphere.

We emphasize that this effect is carried exclusively by ions that stem from the "edges" of the drifting Maxwellian distribution (see Equation 11), that is, they originate far from the peak of the distribution at $u_0 \hat{x}$. The thermal velocity $\sqrt{2k_b T / m}$ is 62 km/s for the upstream hydrogen, 35 km/s for the upstream oxygen, and 24 km/s for the upstream sulfur, that is, a significant fraction of the upstream population does *not* move strictly along the corotation direction and may contribute to surface irradiation along "oblique" trajectories. Therefore, this irradiation effect is purely kinetic in nature and *not* captured by fluid models of Europa's interaction that describe the upstream flow in terms of an averaged velocity \mathbf{u} .

Figures 4a, 4c, and 4e show a reduction in thermal ion flux by 1–8 orders of magnitude close to the equator, near the line where the magnetospheric background field is approximately tangent to the moon's surface. A similar reduction has also been seen in precipitation patterns of *energetic* ions by Breer et al. (2019). Those authors attributed this depletion to the gyration of particles with large field-aligned velocities into

Figure 4. Thermal and energetic ion surface flux by species for case (1). Panels (a), (c), and (e) show the surface flux of thermal ions for the case of perturbed fields (Jovian background field + induced dipole + plasma interaction) for H^+ , O^{2+} , and S^{2+} , respectively, while panels (b), (d), (f), show the flux of energetic H^+ , O^{2+} , and S^{3+} , respectively. Total flux across all species for the case of perturbed fields is shown in panel (g) for the thermal ions and panel (h) for the energetic ions. Total fluxes for the case of only the Jovian background field and the induced dipole (no plasma interaction) are shown in panels (i) and (j). In all plots, west longitude decreases from left to right. The ramside apex is located at 270° W, the wakeside apex at 90° W, the Jupiter-facing apex at $360/0^\circ$ W, and the Jupiter-averted apex at 180° W. Areas with flux less than $10^0 \text{ cm}^{-2} \text{ s}^{-1}$ are plotted in white.

the moon at high latitudes, which gradually depletes the ion population that can reach the near-equatorial region. Fluxes near the equator on the wakeside (around 0° W longitude) are reduced by as much as eight orders of magnitude compared to 60° north or south latitude on the same meridian (Figure 4a). In the trailing hemisphere, the magnitude of the equatorial depletion is less, as the equator is still exposed to the upstream plasma without protection via the solid body of the moon. For thermal hydrogen, this equatorial belt of reduced surface flux is much narrower than for thermal oxygen and sulfur. The small gyroradii of the hydrogen ions compared to the oxygen and sulfur ions allow hydrogen ions with oblique trajectories (i.e., those from the far reaches of the distribution) to reach lower latitudes without gyrating into the moon, a result also seen in energetic ion precipitation patterns by Breer et al. (2019). The ramside flux enhancement for all three species is intersected near the equator by the “belt” of reduced flux, resulting in the two crescent-shaped features with enhanced flux on either side of the equator, centered near 270° W longitude (dark red in Figures 4a, 4c, 4e, and 4g).

In addition to a ram-wake asymmetry, the total thermal ion flux onto the southern hemisphere exceeds that onto the northern hemisphere by as much as one order of magnitude (Figure 4g). This disparity results from the slight inclination of the Jovian background magnetic field in the negative x direction ($\theta_{\text{rot},y} = 11.5^\circ$) and the associated north-south asymmetry in the draping of the field lines around the moon, as shown in Figures 3a and 3d. The magnetic field in the southern hemisphere has a slightly greater southward component than in the northern hemisphere. Therefore, upstream ions that travel into the moon in the north must already have a significant north-south component of their velocity (see Figure 5). It can be seen that the ions that impact the northern hemisphere in Figure 5 enter Europa’s interaction region at a much steeper angle relative to the x -axis than those that impact the south. Therefore, they represent a much less populated portion of the upstream thermal distribution (which is centered at the bulk velocity $\mathbf{u}_0 = u_0 \hat{\mathbf{x}}$, see Equation 11 and Figure 2), than ions hitting the northern hemisphere. For example, a thermal hydrogen ion moving at $u_0 = 100$ km/s with an inclination angle of 60° against the corotation direction x (such as those depicted impacting the northern hemisphere in Figure 5) is weighted 15 times less in the distribution than a hydrogen ion moving purely in the corotation direction. A thermal oxygen ion moving along a trajectory with the same inclination angle is weighted 4,000 times less than if it were traveling along the corotation direction. A thermal hydrogen or oxygen ion traveling at an inclination of 30° (such as those depicted impacting the southern hemisphere in Figure 5) are weighted 2 and 10 times less than their corotating counterparts. Therefore, even if both hemispheres are hit by the same number of macroparticles in our model, macroparticles that impact the north are representative of fewer actual upstream ions than those that impact the south.

A similar north-south asymmetry in surface flux has also been seen by Rubin et al. (2015), who applied a multifluid model to calculate thermal O^+ flux under the upstream conditions observed during the E4 Galileo flyby (see Figure 6 of that paper). During the E4 flyby, the background Jovian field had a positive $B_{x,0}$ component (compared to the negative $B_{x,0}$ modeled here). Rubin et al. (2015) found that thermal oxygen preferentially deposited flux onto the northern hemisphere of Europa. The magnitude of the thermal oxygen flux calculated with our model is also comparable in order of magnitude to the results of Rubin et al. (2015).

The surface flux of thermal hydrogen (Figure 4a) is higher than that of the thermal oxygen by as much as two orders of magnitude (Figure 4c), which is in turn higher than that of the thermal sulfur (Figure 4e) by as much as one order of magnitude. This disparity is strongest in the southern and leading hemispheres. The reason for this difference is the vastly different thermal velocities ($\sqrt{2k_B T / m}$) of the Maxwellian distributions for the three thermal ion species. The thermal velocity of the hydrogen distribution (Figure 2a, blue) is 1.8 times that of the oxygen distribution (red) and 2.5 times that of the sulfur distribution (yellow). This means that, despite having an amplitude $n(m / 2\pi k_B T)^{3/2}$ 25 times smaller than that of oxygen and 50 times smaller than that of sulfur, the hydrogen distribution still exceeds the oxygen and sulfur distributions at velocities sufficiently far from the peak velocity \mathbf{u}_0 . To provide an example, for an ion in the upstream distribution with a speed of $v = u_0$, the thermal hydrogen distribution surpasses the thermal sulfur distribution at an inclination angle of $\sim 60^\circ$ between the particle velocity \mathbf{v} the flow (x) axis, and surpasses the thermal oxygen distribution at $\sim 75^\circ$ inclination. Therefore, the hydrogen distribution contains more particles with velocity vectors highly inclined against the x -axis than either the oxygen or sulfur distributions. Particles depicted in Figure 5 that impact Europa’s northern hemisphere originate in the upstream distribution with an inclination of $\sim 60^\circ$ between their individual \mathbf{v} and the x -axis. This suggests that particles with such highly

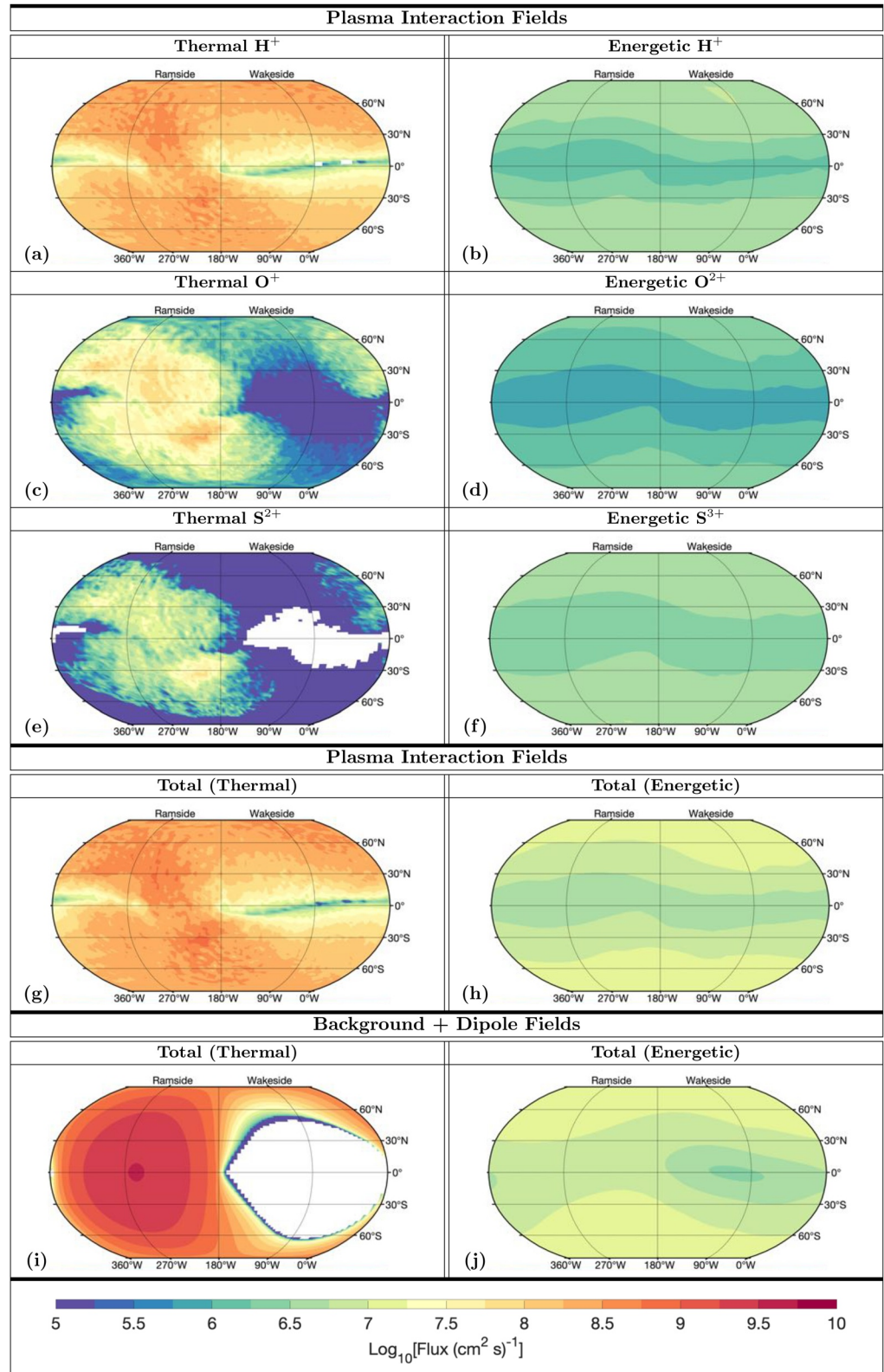


Figure 6. Thermal and energetic ion surface flux for case (2), that is, Europa located at its maximum distance *north* of the center of the plasma sheet. Panels, scales, and orientations are the same as in Figure 4.

inclined velocity vectors \mathbf{v} do make nonnegligible contributions to surface flux. The surface flux imparted by particles moving along highly inclined trajectories allows the hydrogen flux to exceed the sulfur and oxygen fluxes by several orders of magnitude. This phenomenon will be analyzed in more quantitative detail in Section 3.3, where we discuss cases (2) and (3).

Number fluxes of energetic H^+ , O^{2+} , and S^{3+} ions, integrated over the energy range from 5 keV to 10 MeV, are shown in Figures 4b, 4d, and 4f, respectively. In contrast to the thermal flux, which varies across Europa's surface by as much as eight orders of magnitude, the energetic ion flux varies from location to location by no more than half an order of magnitude. For all species, the flux of the thermal plasma onto the ramside exceeds that of the energetic ions by several orders of magnitude. However, the energetic ion flux surpasses the thermal ion flux over a large portion of the wakeside hemisphere, especially near the equator. This is most significant for the energetic sulfur flux, which exceeds the thermal sulfur flux onto the wakeside by up to six orders of magnitude. The large gyroradii of energetic ions compared to the corresponding thermal ions (up to $1.3 R_E$ for 10 MeV S^{3+} ions) allow a large fraction of them to avoid the solid body of Europa and reach the wakeside.

In agreement with the findings of Cassidy et al. (2013), Dalton et al. (2013), and Breer et al. (2019) at Europa and Poppe et al. (2018) at Ganymede, the energetic ion flux is greatest near the poles, as energetic ions with large field-aligned velocities are carried directly into these regions. Since the energetic distribution in this model setup is isotropic, it contains large numbers of such particles moving mostly along the magnetic field. For all three energetic species, the energetic ion flux decreases toward lower latitudes (Figures 4b, 4d, and 4f). Additionally, the depletion of energetic ion flux centered at the equator reaches to much higher latitudes than for the thermal ions, as the gyroradii of the energetic ions are at least an order of magnitude larger than those of the thermal ions. Energetic ions with large field-aligned velocities are therefore much more likely to impact the moon before reaching its equatorial region (see also Breer et al., 2019). Overall, the magnitude of the energetic ion flux onto the surface is greatest for hydrogen, second-greatest for sulfur, and weakest for oxygen. This disparity stems from the fact that the energetic hydrogen differential intensity $I(E)$ in the upstream region exceeds the sulfur intensity by approximately half an order of magnitude at most energies (Figure 2c, blue and yellow, respectively). The differential sulfur intensity, in turn, exceeds the differential oxygen intensity by half an order of magnitude at most energies (Figure 2, yellow and red, respectively).

Energetic ion flux onto Europa's surface for a configuration that includes only the Jovian background field and the induced dipole is shown in Figure 4j. When plasma currents are not included, energetic ion flux onto the ramside apex exceeds that onto the wakeside apex by a factor of 1.5. This flux pattern of energetic ions is similar to the results of Cassidy et al. (2013) and Dalton et al. (2013), who included only a uniform southward magnetic field and no induced dipole. Those authors also calculated the spatial distribution of the total flux of magnetospheric sulfur ions onto Europa's surface, integrated over all energies, and found it to be on the order of 10^7 – $10^8 \text{ cm}^{-2} \text{ s}^{-1}$. This result is in reasonable agreement with our total sulfur flux when neglecting Europa's thermal plasma interaction (plot not shown). Therefore we can conclude that when Europa is near the center of the Jovian plasma sheet, the induced dipole has only a minor quantitative effect on energetic ion surface flux, similar to its role in thermal ion surface flux.

Similar to the results for the thermal ion flux, the energetic ion flux onto the northern hemisphere in Figures 4b–4f is slightly lower than onto the southern hemisphere. The reason for this asymmetry, however, is different from the thermal ions. The (isotropic) upstream distribution of the energetic ions is dependent only upon energy. The north-south asymmetry seen in the energetic ion fluxes is a result of the ~ 100 nT weaker B_z component above the northern polar cap than above the southern polar cap (see Figure 3d), that is, the field lines in the north are more tilted toward downstream than in the south. Energetic particles with large field-aligned velocities therefore impact the northern hemisphere at a more glancing angle than those that impact the southern hemisphere. Since the ion flux onto the surface depends on the angle at which the ions impact (Equation 6), the south receives more ion flux.

Most notable in Figures 4b, 4d, 4f, and 4h is a reduction in the total energetic ion flux near the apex of the trailing hemisphere by half an order of magnitude, compared to the flux onto the leading hemisphere. This is in contrast to what is found by a model that does not include the plasma interaction (Figure 4j), and is

also opposite to the distribution of the thermal ion flux (Figure 4g). A depletion of energetic ion flux above Europa's surface was actually identified with Galileo energetic particle observations from the E12 flyby (Paranicas et al., 2000), which passed within 196 km of Europa's trailing hemisphere. Paranicas et al. (2000) attributed this localized upstream depletion to the gradient drift of energetic ions caused by the pileup of the magnetic field in the trailing hemisphere. The gradient drift velocity is given by

$$\mathbf{v}_\nabla = \frac{mv_\perp^2}{2q|\mathbf{B}|^3}(\mathbf{B} \times \nabla B), \quad (17)$$

where q is the charge of the particle, v_\perp is the velocity of the particle perpendicular to the magnetic field, and ∇B is the gradient of the magnetic field magnitude. Within the ramside pileup region, this gradient points mainly in the positive x direction. Since the magnetic field in our case (1) is mainly oriented in the negative z direction, the resultant gradient drift for positive ions points in the negative y direction, that is, away from Jupiter. Ions that enter the pileup region experience a gradient drift and are deflected away from the moon.

To constrain the contribution of the gradient drift to the ramside depletion in our modeled surface flux, we calculate the deflection of select particles which enter Europa's interaction region while traveling along the x -axis. The magnetic pileup region extends approximately $5 R_E$ upstream. On this length scale, the magnitude of the field changes by ~ 210 nT, from the background value of 418.5 nT at $x = -5 R_E$ to ~ 630 nT directly above the ramside exosphere near $x = -1 R_E$ (see, e.g., Figure 3d). In our case (1), the magnetic field near the center of the pileup region (i.e., at $x = -3R_E, y = 0, z = 0$) is approximately $\mathbf{B} = (-84, 0, -485$ nT). Using these values, we find that a thermal oxygen ion moving at the bulk speed u_0 is deflected by an angle of 0.065° from the x -axis. If such a particle were to begin experiencing nonnegligible gradient drift $3 R_E$ upstream, it would only be deflected by 5 km in the negative y direction. Oxygen ions are deflected the same distance as sulfur ions, and deflected *more* than hydrogen ions. Thus, the deflection of thermal ions via the gradient drift would not be sufficient to prevent them from impacting the moon. Considering the behavior of the three energetic ion species, all at the *same* energy, oxygen would experience the greatest degree of deflection due to the gradient drift. Using the same field parameters, we find that a 100 keV oxygen ion traveling along the x -axis would experience a deflection of 0.72° in the negative y direction. For such an ion to "miss" the moon solely via the gradient drift (i.e., neglecting gyration), deflection would need to commence $80 R_E$ upstream. Even a 10 MeV oxygen ion, which experiences the greatest deflection of any ion modeled in this study, would only be deflected by 7.2° . Upon entering the pileup region, this ion would only be deflected $\sim 0.4 R_E$ off the x -axis, which would not be enough for it to miss the moon's surface. Since the greatest amount of energetic ion flux is deposited by the low energy ions (near 100 keV, see Figure 2c), where the deflection due to the gradient drift is negligible, the mechanism proposed by Paranicas et al. (2000) can only make a minor contribution to the depletion in flux near the ramside.

Instead, we propose a different mechanism that may be most responsible for the depletion in flux of energetic ions onto Europa's ramside hemisphere. The draping of the magnetic field lines around Europa creates a "cocoon" centered near the ramside apex and extending all the way to the poles. When the magnetic field is draped, the surface segment in the ramside hemisphere where the field lines are mostly tangential to the surface is more extended than in the case of a uniform magnetic field. To reach the low ramside latitudes, ions with large field-aligned velocities must therefore travel a much larger distance within one gyroradius of the moon's surface than at the wakeside (where the field lines are not draped). Particles traveling along the draped field lines are therefore very likely to gyrate into the moon's surface prior to reaching the ramside apex.

Our model shows that while Europa is located near the center of the Jovian plasma sheet, *the energetic ion flux onto the surface is lowest where the thermal ion flux is highest*. This disparity is exclusively a result of the electromagnetic field perturbations generated by the interaction between the upstream thermal plasma and the moon's ionosphere and induced dipole, and is therefore *only* present when the plasma interaction is considered.

3.3. Ion Flux Onto Europa at Maximum Distance to the Center of the Plasma Sheet

Figures 6 and 7 display the flux of magnetospheric ions onto Europa's surface for cases (2) and (3), that is, when Europa is located at its maximum distance north and its maximum distance south of the center of the Jovian plasma sheet, respectively. The quantities displayed in each panel are the same as those in Figure 4. Both cases utilize the same upstream thermal and energetic ion distributions (Figures 2b and 2d). The amplitudes of the three thermal ion distributions are lower in this configuration than near the center of the plasma sheet (a result of the lower upstream density). The only difference in upstream parameters between the two configurations is the sign of $B_{y,0}$, which in case (2) is oriented in the *negative* y direction (i.e., away from Jupiter), and in case (3) is oriented in the *positive* y direction (i.e., toward Jupiter).

Similar to case (1), the model shows multiple localized regions of enhanced or reduced ion flux onto Europa's surface. While the shape of these characteristic regions and the magnitude of their respective fluxes are the same in both cases (2) and (3), the different orientation of the background magnetic field causes their locations to be mirrored across the geographic equator ($z = 0$). For example, the enhancement in thermal sulfur flux seen in Figure 6e near 180° west longitude, 30° *south* latitude is mirrored across the equator to 180° west longitude, 30° *north* latitude in Figure 7e. We shall therefore discuss the results of both cases concurrently.

At Europa's farthest distance from the center of the Jovian plasma sheet, the density of the upstream plasma is reduced by a factor of 5 compared to the center of the sheet, and the flux of the thermal population onto the moon's surface is correspondingly weaker. The total thermal flux of all three species in Figures 6 and 7 is lower compared to case (1) by as much as three orders of magnitude, depending on the surface location. Similar to case (1), the thermal ion flux is greatest in the ramside hemisphere.

The surface fluxes of thermal ions under field configurations that include only the induced dipole and the Jovian background field are given in Figures 6i and 7i. These "baseline" flux distributions display a very similar pattern as in case (1): Flux is preferentially deposited around the apex of ramside hemisphere in a "bullseye" pattern, that is, its magnitude decreases uniformly with increasing latitude and longitude away from the ramside apex. The wakeside between 60° north and 60° south receives little to no thermal ion flux. The results shown in Figures 6i and 7i are again qualitatively consistent with the findings of Cassidy et al. (2013) and Dalton et al. (2013) for a uniform southward field, an indication that even when the inducing field is at its maximum strength (as it is in cases [2] and [3]), the induced dipole alone still does not significantly affect the thermal ion flux onto Europa's surface. This finding is consistent with Breer et al. (2019), who showed that only near-equatorial latitudes is the dipole alone able to cause a discernible drop of the *energetic* ion flux. At Europa, the horizontal (inducing) component of the Jovian background magnetic field is (at maximum) approximately *half* as strong as the (noninducing) north-south field component (Kivelson et al., 1999; Zimmer et al., 2000). Therefore, the induced field never reaches the strength necessary to significantly modify thermal ion surface flux. This is in stark contrast to ion precipitation onto Callisto, where the inducing field component can be up to 3–5 times the magnitude of the non-inducing field component, and the induced dipole therefore has a strong influence on ion precipitation even in the high-energy regime (Liuzzo et al., 2019b).

Similar to case (1), when the thermal plasma interaction is considered (Figures 6 and 7, panels (a), (c), (e), and (g)), deflection of thermal ions around the Alfvén wings reduces the flux onto the ramside by over an order of magnitude compared to when the plasma interaction is not taken into account. The greatest amount of flux is still deposited close to the ramside apex. However, the wakeside now receives a surface flux of up to $10^{7.5} \text{ cm}^{-2} \text{ s}^{-1}$, compared to nearly zero when the plasma interaction is not considered. As in case (1), the field perturbations allow a certain portion of the upstream particles (originating from the "outer" reaches of the Maxwellian distribution) to reach the wakeside hemisphere: the trajectories of these particles may intersect the draped field lines and subsequently be deflected back into the moon, analogous to Figure 5. However, at this large distance to the center of the plasma sheet, the Alfvénic Mach number ($M_A = 0.33$) is only *half* of its maximum value at the center of the plasma sheet ($M_A = 0.66$). Therefore, the draping of the field lines is significantly weaker: the Alfvén wing characteristics are inclined by only 18° against the background field \mathbf{B}_0 , compared to 33° near the center of the plasma sheet. This results in a stronger north-south component (B_z) of the magnetic field near the moon than in case (1). Similar to the southern hemisphere

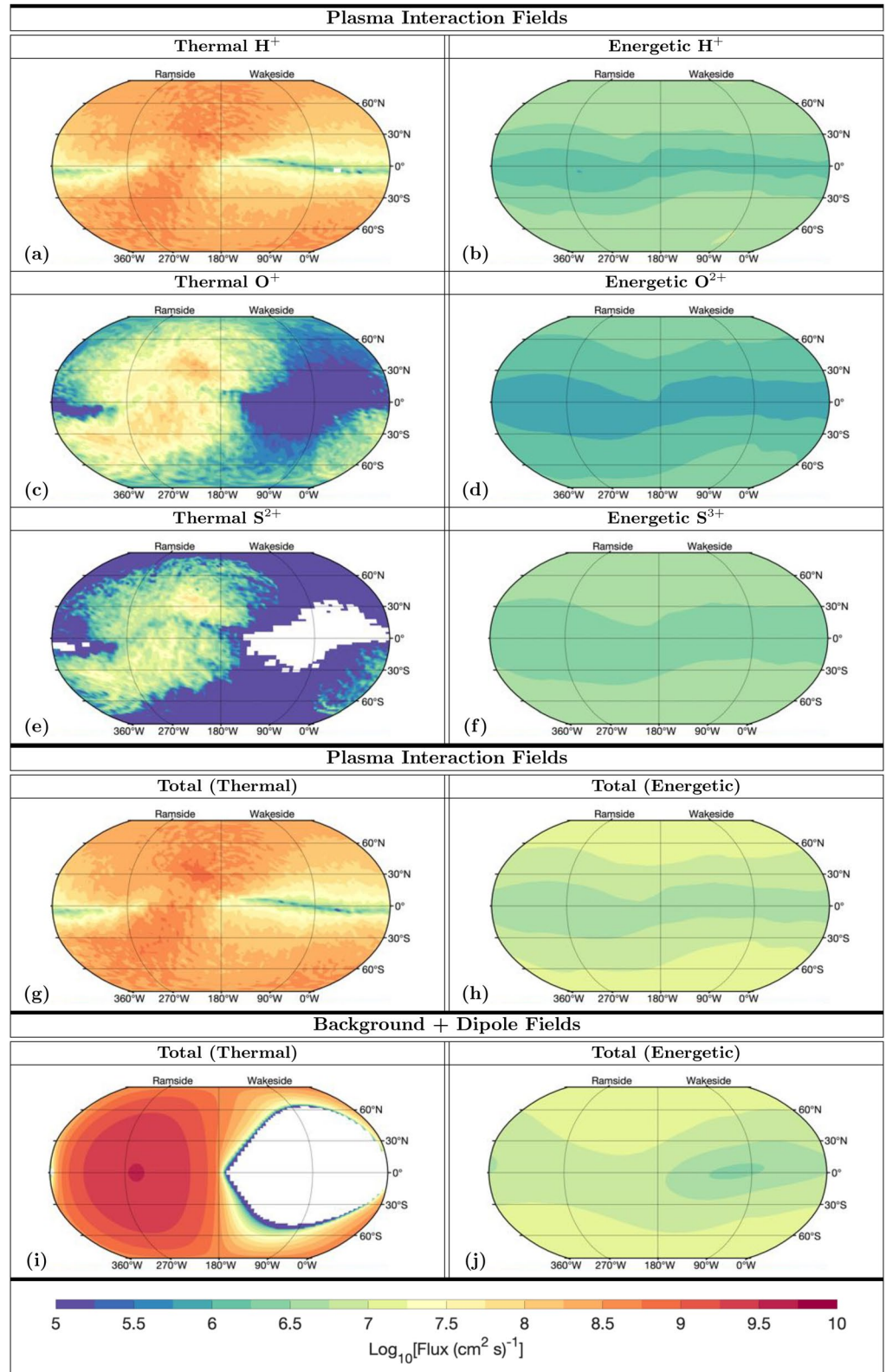


Figure 7. Thermal and energetic ion surface flux for case (3), that is, Europa located at its maximum distance *south* of the center of the plasma sheet. Panels, scales, and orientations are the same as in Figure 4.

trajectories in Figure 5, particles with largely flow-aligned velocities are carried nearly along the \tilde{z} (case (2)) or z^* axis by the strong B_z component into the moon's polar caps. This northward/southward movement of thermal particles allows significant ion flux onto the leading hemisphere surface. Only near the equator, where particles moving northward or southward impact tangentially to the surface, is the flux significantly reduced.

The inclusion of the plasma interaction currents “smears” out the ramside bullseye pattern, redistributing thermal ion flux across the surface and reducing the magnitude of the associated ion flux near the upstream apex by 2–3 orders of magnitude (Figures 6 and 7, panels (a), (c), and (e)). The thermal velocity (width) of the hydrogen distribution in this configuration ($\sqrt{2k_B T / m} = 62$ km/s) is 62% of the bulk velocity ($u_0 = 100$ km/s), much greater than the thermal velocity of the oxygen and sulfur distributions (35 km/s and 24 km/s, respectively). This means that, in contrast to oxygen and sulfur, a significant fraction of the hydrogen ions approach Europa with large field-aligned velocities (i.e., on trajectories highly inclined against the bulk flow direction). Since particles moving along such highly inclined trajectories are able to precipitate onto the surface at any latitude and even in the wake, hydrogen ions can irradiate the majority of Europa's surface. Because the distributions of the thermal oxygen and sulfur ions are much narrower, the bulk of these ions travel nearly in alignment with the corotational flow direction. This means that the flux of the two heavy upstream species (Figures 6 and 7, panels (c) and (e)) is largely concentrated in the ramside hemisphere, where the majority of particles with velocities nearly aligned with the flow axis impact the surface.

The dominance of thermal hydrogen flux over the flux of the two heavy thermal species can be explained if hydrogen ions from the “far reaches” of the distribution can make a similarly strong contribution to surface flux as heavy ions near the peak of their distributions. To constrain the role of ions with highly inclined trajectories in determining surface fluxes for the three species studied here, we calculate the number density of particles that populate various regions in velocity space for each thermal distribution. To facilitate the required integrations, we first introduce the quantity $\tilde{\mathbf{v}} = \mathbf{v} - \mathbf{u}_0$, thereby centering the distributions at a value of $\tilde{\mathbf{v}} = 0$. The hydrogen distribution exceeds the heavy ion distributions at a certain speed \tilde{v}_{crit} , which is different for oxygen and sulfur: $\tilde{v}_{crit,O^+} = 0.73 u_0$ and $\tilde{v}_{crit,S^{2+}} = 0.5 u_0$, respectively. We can therefore define a “central region,” located between $|\tilde{\mathbf{v}}| = 0$ and $|\tilde{\mathbf{v}}| = \tilde{v}_{crit}$, where the respective heavy-ion distribution dominates. Since the isosurfaces of the 3D Maxwellian distributions (Equation 11) are spheres in velocity space, we can then calculate the number density within the central region by integrating the distribution function in polar coordinates from $|\tilde{\mathbf{v}}| = 0$ to $|\tilde{\mathbf{v}}| = \tilde{v}_{crit} = |\mathbf{v}_{crit} - \mathbf{u}_0|$. The integral becomes

$$n_{central} = 4\pi \int_0^{\tilde{v}_{crit}} f(\tilde{\mathbf{v}}) \tilde{v}^2 d\tilde{v} \quad , \quad (18)$$

where $f(\tilde{\mathbf{v}})$ is the thermal ion distribution as a function of $\tilde{\mathbf{v}}$. The spherical symmetry of the distribution around $\tilde{\mathbf{v}} = 0$ reduces the angular component of the velocity integral to a factor of 4π . The number density of particles outside the central region, n_{outer} , can be found by subtracting $n_{central}$ from the total upstream density for each species, given in Table 1. We find that within the region where the oxygen distribution is above the hydrogen distribution, the oxygen ions have a density $n_{central} = 21$ cm⁻³, while for hydrogen ions $n_{central} = 3.43$ cm⁻³. Outside this central region, however, the oxygen ions have a density n_{outer} of only 0.6 cm⁻³, while the hydrogen ions have a density n_{outer} of 2.57 cm⁻³, more than four times the oxygen density. Similarly, within the region where the sulfur distribution is above the hydrogen distribution, the sulfur ions have a density $n_{central} = 11.5$ cm⁻³, while for the hydrogen ions $n_{central} = 1.66$ cm⁻³. Outside the central region, the sulfur density n_{outer} is 0.4 cm⁻³, while the hydrogen density n_{outer} is 10 times larger at 4.34 cm⁻³. Therefore, while the heavy species dominate in the central region by a factor of 5–10, the hydrogen dominates *outside* the central region by a similar factor. For the two heavy species, n_{inner} is not even an order of magnitude greater than n_{outer} of the hydrogen ions. Also taking into account the different deflection patterns of protons and heavy species in the perturbed fields, it is therefore plausible that protons with highly inclined trajectories can make a similar contribution to surface flux as heavy ions (oxygen and sulfur) traveling close to the flow direction. The magnitude of the surface flux deposited by thermal hydrogen ions can therefore match that of the thermal heavy ions, despite the significantly lower amplitude of the hydrogen distribution. We

emphasize that we calculate surface *number* fluxes $n\mathbf{u}$ for each species. Thus, in contrast to, for example, surface *energy* fluxes, the modeled fluxes are *not* weighted with the particle masses.

Due to the important role of thermal ions that approach Europa along inclined trajectories, in combination with the complex deflection of these particles in the perturbed fields, the relative magnitudes of the surface number flux of each thermal species do indeed follow the width (i.e., the thermal velocity) of the upstream distributions, rather than their amplitudes. In other words, the relative fluxes of the three thermal species are determined by the contribution of non-flow aligned particles. Overall, the hydrogen flux exceeds the oxygen flux by up to three orders of magnitude, and the oxygen flux exceeds the sulfur flux by up to one order of magnitude (Figures 6 and 7, panels (b), (d), and (f)). The dominance of thermal hydrogen ion surface flux compared to the thermal oxygen and sulfur flux is strongest near the poles (Figures 6 and 7, panels (a), (c), and (e)). Since the field lines near the moon in cases (2) and (3) are nearly perpendicular to the flow axis, particles (partially) following the field lines are preferentially deflected into the polar regions (analogous to Figure 5, southern hemisphere).

The addition of a strong negative $B_{y,0}$ component to the background field brings case (2) close to the field configuration of the Galileo E4 flyby, which made its closest approach to Europa when it was located well north of the center of the plasma sheet. Our resulting flux map for thermal oxygen ions (Figure 6c) is both qualitatively and quantitatively similar to that calculated by Rubin et al. (2015) using the upstream conditions measured during E4 (see Figure 6 of that work). Those authors found the flux to be concentrated in a region centered at the ramside apex and extending northwards and southwards along the background magnetic field. Their multifluid model also revealed two “islands” of enhanced flux: One near 200° west longitude and 30° south latitude, and the other near 300° west longitude and 30° north latitude. The morphology and absolute values in this thermal oxygen flux pattern are consistent with the output of our model, as displayed in Figure 6c.

The magnitudes of the *energetic* ion flux onto Europa’s surface for the three species (Figures 6 and 7, panels (b), (d), and (f)) are much more similar to each other in this configuration than in case (1). At any given location on Europa’s surface, the greatest difference in flux between energetic protons, oxygen ions, and sulfur ions is only approximately a factor of 1.5–2. The reason for this similarity lies mainly in the upstream energy distributions $I(E)$ (Figure 2d) of the three species. The difference between the three energetic distributions $I(E)$ at any energy (Figure 2d) is much smaller than at the center of the plasma sheet (Figure 2c). The upstream distributions of energetic oxygen and sulfur in cases (2) and (3) are only a factor of 2 different near the energy where they are maximized (10–100 keV), and remain within a factor of 3 at all energies. In case (1), the oxygen and sulfur distributions differ by a factor of 3–4 at their maximum energy, and by a factor of approximately 4 at all other energies. Similarly, in cases (2) and (3), the hydrogen intensity is an order of magnitude greater than the oxygen and sulfur intensities near its maximum at 10 keV, but falls below the sulfur distribution near 100 keV. The hydrogen distribution in case (1) does not fall below the oxygen or sulfur distributions at any energy. Due to the stronger similarity of the three upstream energetic distributions in cases (2) and (3), the energy-integrated surface fluxes of all three ion populations (Figures 6 and 7, panels (b), (d), and (f)) are far more uniform between species than in case (1), where the hydrogen flux exceeds the heavy ion flux by 1–2 orders of magnitude.

Similar to when Europa is near the center of the Jovian plasma sheet, the polar regions receive an order of magnitude greater total energetic ion flux than the equator (Figures 6h and 7h). The “Breer belt” of reduced flux along the equator is evident for all three ion species in these field configurations as well (Figures 6 and 7, panels (b), (d), (f), and (h)), although the deviation of the belt from the equator has increased compared to case (1). This enhanced deviation is mostly a result of the greater inclination of the Jovian background field against the z -axis, which pulls the line where the background field is tangent to the surface farther from the equator near the Jupiter-facing and Jupiter-averted apices (see Section 3.2 of Breer et al. (2019) for a more in-depth explanation of this).

The ramside depletion in energetic ion flux found near the center of the Jovian plasma sheet (Figures 4b, 4d, 4f, and 4h) is less pronounced when Europa is located far north or south of the center of the sheet. Since the magnetic field is not as strongly draped around the moon (Figures 3b, 3c, 3e, and 3f), energetic particles moving along the field lines travel a shorter distance within one gyroradius of the surface than in case (1).

Compared to case (1), these ions are therefore more likely to reach low ramside latitudes before gyrating into the moon.

In addition, the magnitude of the magnetic field gradient in Europa's ramside pileup region is reduced to two-thirds of its strength in case (1), and the magnetic field magnitude $2 R_E$ upstream of the ramside apex is decreased by 13 nT ($\mathbf{B} = (0, \pm, -426 \text{ nT})$, cases (2) and (3), respectively). Looking at Equation 17, the gradient drift velocity for an ion of the same species and energy is reduced by 57% compared to case (1). Using a similar calculation as in Section 3.2, we find that a 100 keV oxygen ion traveling along the x -axis is only deflected by 48.7 km ($0.032 R_E$) when passing through the pileup region, while a 10 MeV oxygen ion is deflected by 480 km ($0.3 R_E$). Therefore, the role of the local gradient drift in protecting the ramside hemisphere is even weaker when Europa is far from the center of the plasma sheet.

Due to the reduced field line draping and the weaker gradient drift, there is no "inverted bullseye" pattern (quasi-circular region of reduced energetic ion flux) near the ramside apex as there was in case (1). However, despite the lower Alfvénic Mach number in cases (2) and (3), the plasma interaction does still reduce energetic ion flux onto Europa's ramside apex by a factor of 2–3 (Figures 6 and 7, panel (h)), compared to when only the Jovian background field and the induced dipole are considered (Figures 6 and 7, panel (j)).

The equatorial region in the wakeside hemisphere receives a slightly greater degree of protection from energetic ions when Europa is located far from the center of the plasma sheet. In case (1), energetic ion flux onto the wakeside equatorial region is only reduced by a factor of 1.5–2 (Figures 4b, 4d, and 4f) compared to the poles, whereas in cases (2) and (3) it is reduced by a factor of 3–4 (Figures 6 and 7, panels (b), (d), and (f)). When Europa is at its maximum distance from the center of the plasma sheet, the magnitude of the induced dipole field is 2.5 times stronger than at the center. Breer et al. (2019) showed that a dipole of this strength is able to provide slightly increased protection from energetic ion flux near the equator by enhancing the tangential component of the magnetic field near the surface at high latitudes. This increases the likelihood that energetic ions following the field lines will gyrate into the moon at higher latitudes before reaching the equatorial region. Near the ramside this protection supplements the protection due to the field line draping. The combination of weaker field line draping (which reduces the protection of the ramside apex from energetic ion flux) and the strengthened dipole (which slightly enhances protection around the wakeside equator) results in a more uniform equatorial surface flux from energetic ions compared to case (1).

Overall, the shielding effect against energetic ion flux provided by the field perturbations is significantly weakened when Europa is located far from the center of the Jovian plasma sheet. At these large distances, the field line draping is too weak to provide the same degree of protection against energetic ion flux that they do at the center of the sheet.

3.4. Time-Averaged Ion Flux Over a Complete Synodic Rotation and Consequences for Europa's Surface and Exosphere

We now investigate the spatial distribution of ion flux across Europa's surface, averaged over an *entire* synodic rotation. To determine this quantity, we average the surface flux maps of cases (1)–(3). Europa spends more time near its peak distance north or south of the plasma sheet than near the center of the sheet. However, the moon also passes through the center of the plasma sheet *twice* during each synodic rotation. Therefore, the weights that should be assigned to each of the three cases to determine the averaged flux pattern are not exactly equal and are difficult to constrain. We tested various scenarios which either assign equal weights to cases (1)–(3), or emphasize cases (2) and (3), that is, Europa located at large distances to the center of the plasma sheet. We found that the averaged surface flux patterns do not begin to qualitatively change until cases (2) and (3) are weighted eight times higher than case (1), a scenario that we judge to be unphysical. For the time-averaged surface fluxes discussed in this section, we therefore assigned equal weights to cases (1)–(3).

Figure 8 displays the magnetospheric ion flux onto Europa's surface, averaged over an entire synodic rotation. The first row (panels (a–c)) displays maps of the time-averaged flux when only the Jovian background field and Europa's induced dipole are taken into account, while the second row (panels (d–f)) displays the time-averaged flux when the influence of the plasma interaction is also considered. The third row (panels (g–i)) contains plots of ion flux as a function of west longitude for select latitudes: along the equator (0° ,

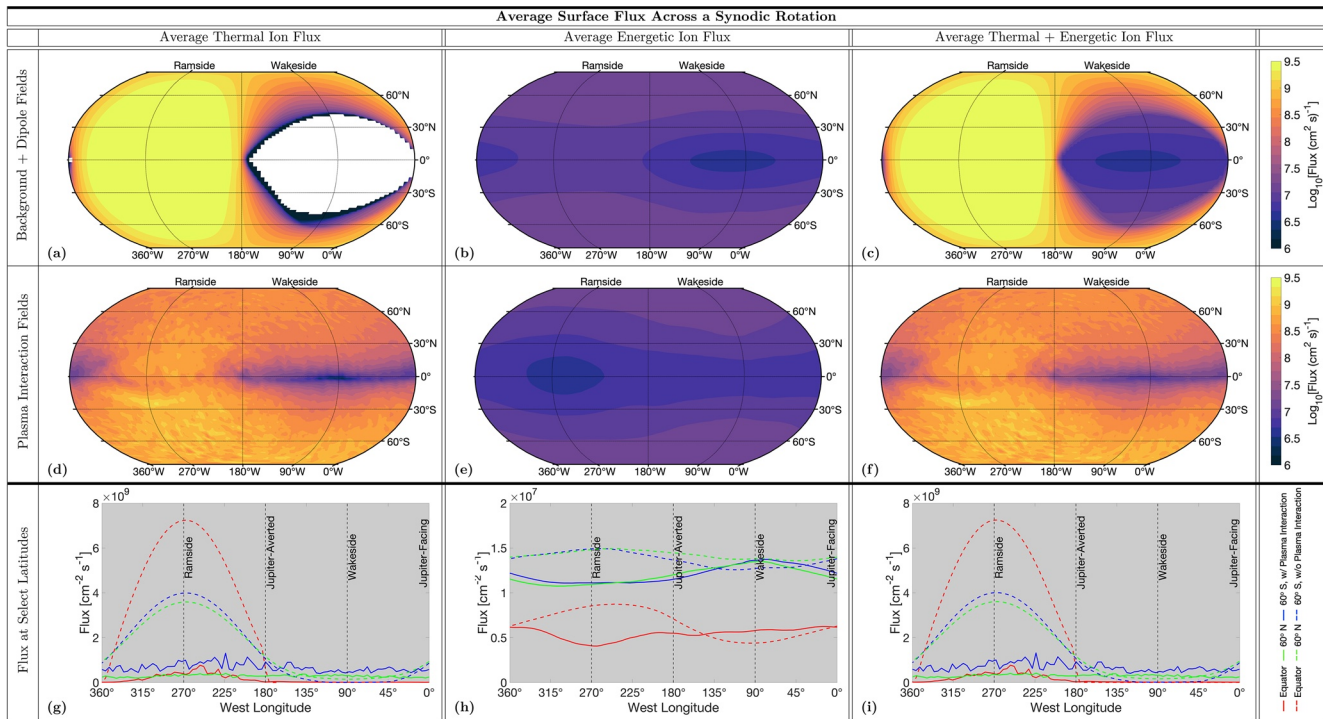


Figure 8. Ion number flux onto Europa’s surface, averaged across an entire synodic rotation period. The first column (panels (a), (d), and (g)) displays the surface flux of thermal ions only, the second column (panels (b), (e), and (h)) displays the surface flux of *energetic* ions only, and the third column (panels (c), (f), and (i)) displays the total ion surface flux (thermal and energetic ions). The first row (panels (a)–(c)) displays ion surface flux when only the Jovian background field and Europa’s induced dipole are considered. The second row (panels (d)–(f)) displays ion surface flux when the plasma interaction is also taken into account. The third row plots ion flux versus west longitude at given latitudes: 0° (red), 60° N (green), and 60° S (blue). Dashed lines represent the surface flux when the plasma interaction is not considered, while solid lines represent surface flux when the plasma interaction is considered.

red), 60° N (green), and 60° S (blue). In these three panels, the dashed lines represent surface flux when the plasma interaction is *not* considered, while the solid lines represent flux when the plasma interaction is taken into account. The first column (panels (a), (d), and (g)) displays the averaged surface flux of thermal ions only, the second column (panels (b), (e), and (h)) displays the averaged surface flux of energetic ions only, and the third column (panels (c), (f), and (i)) displays the combined flux of thermal and energetic ions.

Many of the features found in the individual cases (1)–(3) are also discernible in the maps of the time-averaged flux. For instance, the trailing hemisphere receives the greatest amount of thermal ion flux (Figures 8a, 8d, and 8g), although draping of the field lines due to the plasma interaction causes the leading hemisphere to be heavily irradiated as well. When the plasma interaction is included, deflection of thermal ions around the Alfvén wings reduces the flux onto the trailing hemisphere by several orders of magnitude compared to when only the Jovian background field and induced dipole are considered (Figures 8d and 8g). When the plasma interaction is considered, the thermal ion flux onto the high-latitude surface is nearly uniform at all longitudes (Figure 8d, solid green and blue lines in Figure 8g), while at the equator the thermal flux sharply drops in the leading hemisphere (Figure 8d).

The averaged flux of energetic ions is greatest near the poles, both without and with the plasma interaction (Figures 8b and 8e, respectively), as the high field-aligned velocities of many particles within the energetic population allow them almost unrestricted access to these areas. When the plasma interaction is considered, the region of minimum energetic ion flux shifts along Europa’s equator from the leading hemisphere to the trailing hemisphere (Figure 8e). The draping of the field lines around the moon causes high-energy ions to gyrate into the surface before they can reach the trailing hemisphere apex. Between 60° north and 60° south latitudes, the plasma interaction *reverses* the longitudinal gradient of energetic ion surface flux (Figure 8h): at longitudes where the energetic surface flux *increases* when the plasma interaction is *not* considered, it *decreases* when the plasma interaction is considered, and vice versa.

Due to their smaller gyroradii, this mechanism is likely far less efficient at protecting the trailing hemisphere apex from bombardment by energetic electrons. However, the motion of energetic electrons is far more complex than that of ions, as the rapid bounce motion of electrons between Jupiter's magnetic poles allows them to make multiple "attempts" to impact Europa's surface (Paranicas et al., 2009). Precipitation of such "returning" electrons has been found to play a significant role in electron surface bombardment of Callisto (Liuzzo et al., 2019a) and Ganymede (Liuzzo et al., 2020). However, the modeling of this bounce motion requires implementation of a complete, global model of the Jovian magnetosphere, which represents a significant modification of the framework applied here. We therefore leave the calculation of electron surface fluxes at Europa to future work.

The combined thermal *and* energetic ion number flux (Figures 8c, 8f, and 8i) is still dominated by the contribution of the thermal ions, except at low latitudes on the leading hemisphere. Here, the surface flux of the energetic ions is most significant. For example, when the plasma interaction is not considered, the flux of energetic ions (Figure 8b) onto the leading hemisphere between 30°N and 60°S (which is almost completely shielded from thermal ion flux, see Figure 8a), makes a contribution to the total flux that is more than seven orders of magnitude greater than that of the thermal ions. When the plasma interaction is included, the thermal plasma can impinge on the leading hemisphere at all latitudes (Figure 8d), and therefore the flux of energetic ions (Figure 8e) makes a similar contribution to the total flux (Figure 8f) only near the leading hemisphere equator. The polar caps of Europa receive high levels of irradiation from both the thermal ($\approx 10^9 \text{ cm}^{-2} \text{ s}^{-1}$) and energetic ions ($\approx 10^{7.5} \text{ cm}^{-2} \text{ s}^{-1}$), independent of the presence of the plasma perturbation. With the plasma interaction included, the flux of thermal ions exceeds that of energetic ions by 1.5–3 orders of magnitude everywhere except near the wakeside low latitudes.

We now explore the consequences of our modeled ion irradiation patterns for weathering of Europa's surface ice. The presence of Europa's subsurface ocean and its possible influence on surface composition (e.g., Doggett et al., 2009; Squyres et al., 1983) have made it of paramount importance to understand which materials on the surface are exogenic in origin (i.e., originating from Europa's space environment), and which are endogenic (i.e., originating from beneath Europa's surface). Multiple studies have suggested that magnetospheric ions, especially sulfur, are important agents in weathering of Europa's surface (e.g., Carlson et al., 2005; Dalton et al., 2012; Hendrix et al., 2011). Sulfur is of special interest, as its presence in both the magnetospheric environment (originating from Jupiter's volcanic moon Io) *and* in subsurface brines means that sulfur deposits on the surface could be *either* exogenic *or* endogenic in origin. Sulfur deposits on the surface have also been hypothesized to be the darkening agents responsible for noticeable low-albedo regions, such as those observed by Galileo near the trailing hemisphere apex (e.g., Carlson et al., 1999; McEwen, 1986).

Laboratory studies, such as that by Strazzulla et al. (2007), have shown that implantation of sulfur ions into water ice can efficiently produce sulfuric acid (H_2SO_4), which has been detected on Europa's surface (e.g., Dalton et al., 2012; Paranicas et al., 2001) by the Galileo Near-Infrared Mapping Spectrometer (NIMS, Carlson et al. (1992)). Understanding which regions receive significant sulfur ion flux can help to identify areas where surface materials are exogenically derived. Several previous studies have attempted to correlate the strong surface gradients in sulfuric acid concentration detected by Galileo to magnetospheric particle bombardment (e.g., Paranicas et al., 2001; Patterson et al., 2012; Shirley et al., 2010).

Dalton et al. (2013) investigated the role of nonuniform charged particle bombardment in surface weathering and radiolysis, focusing especially on the spatial variation of sulfuric acid concentrations across Europa's surface. Those authors used the model of Cassidy et al. (2013) to calculate the spatial distribution of ion surface flux. As an approximation, the magnetic field was assumed to be uniform and southward, that is, the induced dipole and the interaction of the moon with the upstream plasma were not considered. In addition, the role of Europa's time-varying local magnetospheric environment in shaping the ion surface flux pattern was assumed to average out over a synodic rotation period (see also Cassidy et al., 2013). Surface concentrations of sulfuric acid were taken from NIMS measurements of a diverse range of terrains and features (given in Table 2 of Dalton et al. (2013), and illustrated in their Figure 1). These measurements sampled discrete locations on the ramside, Jupiter-averted, and wakeside hemispheres, ranging from 60°S to 20°N. While the surface area covered by these measurements is rather limited, more expansive observations by future missions, such as the JUICE or Europa Clipper spacecraft, will soon provide additional surface

concentration measurements to substantiate possible correlations to our modeled surface fluxes. Dalton et al. (2013) then correlated these measurements of the sulfuric acid concentration with their modeled particle fluxes at each respective location. A strong, positive correlation was found between sulfuric acid surface concentration and both electron *energy* flux (correlation coefficient $r \approx 0.75$) and sulfur ion *number* flux ($r = 0.93$).

Dalton et al. (2013) hypothesized that precipitating magnetospheric electrons impart energy onto the surface, heating it and thereby allowing incident sulfur ions to implant more deeply. The correlation of sulfuric acid concentrations and the influx pattern of magnetospheric sulfur ions led these authors to suggest that the sulfur bound in the sulfuric acid on Europa's surface is predominantly exogenic in origin. However, in several regions, the observed sulfuric acid concentrations were lower than their proposed trend. They reasoned that in surface locations that receive high levels of sulfur flux but have low sulfuric acid levels, endogenic sulfur might be present.

However, we have shown that the inclusion of the field perturbations near Europa drastically alters ion surface flux patterns. For instance, our results reveal significant thermal ion flux (up to $10^8 \text{ cm}^{-2} \text{ s}^{-1}$) onto the leading hemisphere when the plasma interaction is considered (Figure 8d), where the model of Dalton et al. (2013) predicts the thermal ion flux to be *zero* (see Figure 11 of that paper). In addition, we have shown that the trailing hemisphere apex receives the *lowest* amount of energetic ion flux (Figure 8e), where Dalton et al. (2013) suggest that energetic ion flux is *maximized*. The vast differences between our flux patterns (obtained for perturbed fields) and the patterns calculated by Dalton et al. (2013) for uniform fields strongly suggest that Europa's plasma interaction plays a critical role in any search for correlations between the moon's surface composition and the particle influx from its space environment. Based on the same Galileo observations used by Dalton et al. (2013), we therefore investigate possible correlations to our modeled flux patterns.

To accomplish this, we plot the sulfuric acid concentration observed at various surface locations versus our modeled average sulfur ion number flux (Figures 9a and 9b) and versus averaged total ion number flux (hydrogen + oxygen + sulfur, Figures 9c and 9d). Figures 9a and 9c utilize flux values calculated considering only the Jovian background field and the induced dipole, while Figures 9b and 9d use flux calculated with the plasma interaction included. The total ion number fluxes used for this analysis are also displayed in Figures 8c and 8f. An analogous study of the correlation between surface ion *energy* flux and measured sulfuric acid concentrations is illustrated in Figure 10. We use the same concentration measurements as Dalton et al. (2013). For each case, a linear fit to the values is included (black, dashed line) to guide the reader's eye.

Our results show that the inclusion of the time-varying Jovian background field and Europa's induced dipole alone already slightly reduces the correlation between sulfur ion flux onto the surface and observed sulfuric acid concentrations ($r = 0.82$, Figure 9a), compared to $r = 0.93$ reported by Dalton et al. (2013). However, the general trend in our results is still an (approximately) linear increase in sulfuric acid concentration with increasing sulfur flux. Although many data points in Figure 9a are similar to those found by Dalton et al. (2013), several important features shift their position in the diagram relative to the general trend. Most notably, Dalton et al. (2013) found that the "low-albedo plains," located near 180°W , 30°S (red dots), fell *below* the general trend, that is, have a lower concentration of sulfuric acid than the sulfur flux at the respective location would indicate. These authors hypothesized, similar to Shirley et al. (2010), that these regions are younger, and therefore have been exposed to less cumulative sulfur irradiation, resulting in lower levels of sulfuric acid. However, we find that even when only the time-varying Jovian background field and Europa's induced dipole are considered, most of these points move *above* the linear fit between sulfur ion flux and sulfuric acid concentration (Figure 9a). Thus, their sulfuric acid levels are actually *higher* than the sulfur flux at their respective location would indicate. Therefore, the relative youth of these features does not seem to have a straightforward effect on the sulfuric acid concentration at their locations. When only the Jovian background field and Europa's induced dipole are considered, the total flux of *all* ions (Figure 9c) has a slightly higher correlation to sulfuric acid concentrations on the surface ($r = 0.84$) than the flux of sulfur ions alone. However, we note that the substantial effect of the plasma interaction has not been considered in Figures 9a and 9b, so these results are still based on an incomplete picture of ion surface flux.

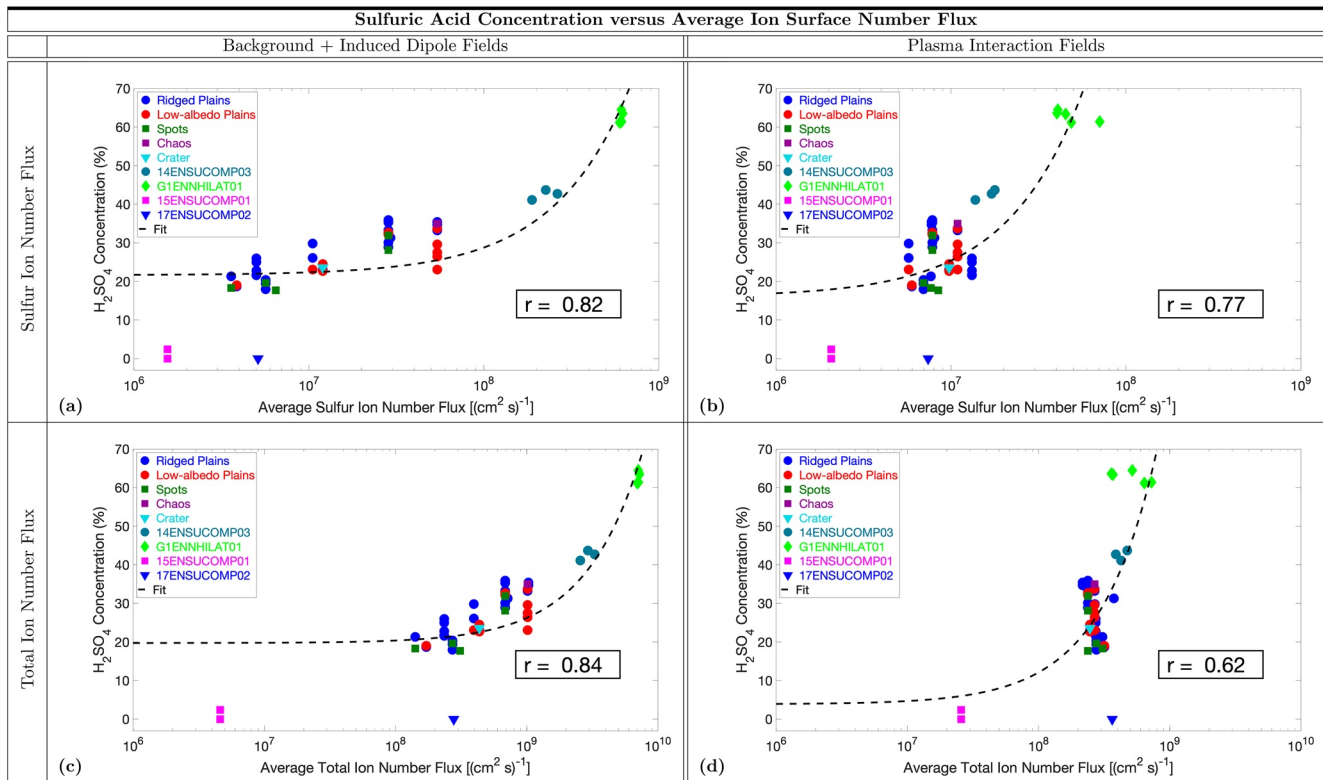


Figure 9. Sulfuric acid concentration as measured at various locations on Europa’s surface by the Galileo spacecraft versus sulfur ion flux (first row, panels (a) and (b)), and total ion flux (second row, panels (c) and (d)), as obtained by our model. Different markers denote different locations on Europa’s surface, see Dalton et al. (2013) for a description of these locations and measurements. The first column (panels (a) and (c)) denotes ion surface flux when only the Jovian background field and Europa’s induced dipole are considered, while the second column (panels (b) and (d)) denotes surface flux when the plasma interaction is also taken into account. A linear fit to the sulfuric acid concentration measurements and each respective ion flux is given as a dashed, black line. Note that the linear fit appears curved in these plots, as the horizontal axis is plotted on a logarithmic scale. The correlation coefficients between the observed sulfuric acid concentrations and respective ion flux, r , are also given.

We therefore investigate the same sulfuric acid concentration measurements and sulfur ion flux computed with the effect of the thermal plasma interaction included (Figure 9b). These results take into account the complete picture of Europa’s magnetospheric environment. Remarkably, despite the clear alterations to surface flux patterns imposed by the plasma interaction, a strong, positive correlation between sulfuric acid concentration and sulfur ion flux remains ($r = 0.77$). However, it is significantly weaker than the correlation found by Dalton et al. (2013) using a uniform, southward magnetic field ($r = 0.93$). The distribution of data points in Figure 9b is more clumped together (covering a flux range of approximately 15 million ions/($\text{cm}^2 \text{ s}$)) compared to Figure 9a, where the flux values at these same locations span a range of ~ 60 million ions/($\text{cm}^2 \text{ s}$). The clustering of data points in Figure 9b is a result of the significantly more uniform sulfur ion flux across Europa’s surface when the plasma interaction is considered. The most prominent examples of the weakened correlation are observations of the sulfuric acid concentrations in the region near 200°W , 20°N (labeled 14ENSUCOMP03, turquoise dots in Figure 9b). When the plasma interaction is *not* considered (Figure 9a), these regions receive almost as much as an order of magnitude higher sulfur flux than any of the ridged plain or low-albedo plain regions near 180°W , 30°S (blue and red dots, respectively). However, when the plasma interaction is included (Figure 9b), the regions labeled 14ENSUCOMP03 receive a largely comparable amount of sulfur flux to both the ridged plain and low-albedo plain regions.

When the plasma interaction is included, the correlation between sulfuric acid levels observed on the surface and ion flux of all species (Figure 9d) drops to $r = 0.62$. This result makes physical sense, as a strong correlation between sulfuric acid concentration and hydrogen ion flux is not expected. The remaining correlation in Figure 9d is likely a result of only the contribution of the heavy ions (oxygen and sulfur) to the

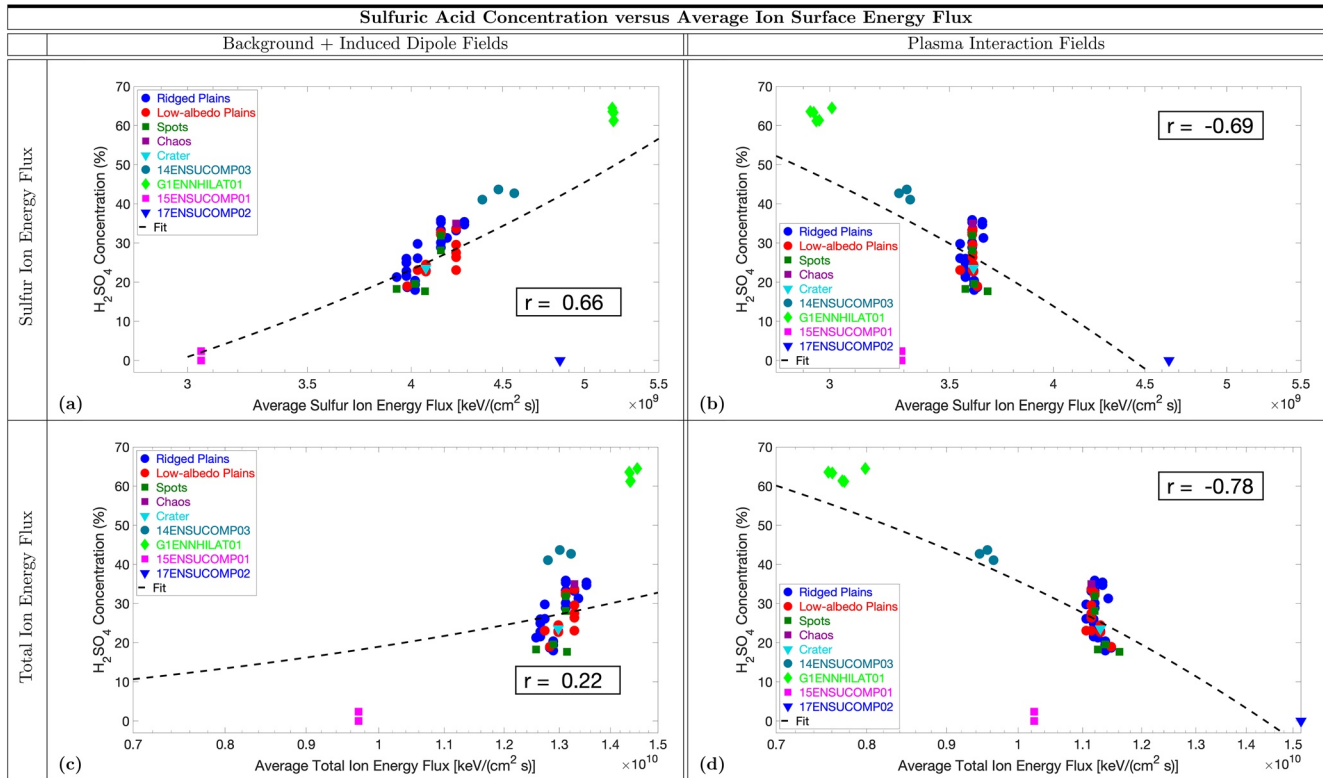


Figure 10. Sulfuric acid concentration as measured at various locations on Europa’s surface by the Galileo spacecraft versus sulfur ion energy flux (first row, panels (a) and (b)), and total ion energy flux (second row, panels (c) and (d)), as obtained by our model. The layout of the panels, as well as the markers representing different surface sulfuric acid measurements, are the same as in Figure 9. Similar to Figure 9, a linear fit is superimposed on each plot as a dashed black line, and the correlation between the respective ion flux and the measured surface concentrations r is given.

total ion flux. This result underscores the importance of including a complete picture of the perturbed electromagnetic fields when calculating ion surface flux: without the perturbations, a stronger correlation exists between measured sulfuric acid concentrations and the flux pattern of *all* ions than between sulfuric acid concentrations and the flux of *sulfur* ions alone.

The nearly uniform pattern of the total ion number flux shown in Figures 8f and 8i does *not* imply a lack of correlation with the markedly non-uniform sulfuric acid surface concentrations given by Dalton et al. (2013), which were found to peak near the ramside apex. The total ion flux is dominated by the contribution of magnetospheric hydrogen ions, which irradiate nearly every location on Europa’s surface (Figures 4a, 6a, and 7a). However, hydrogen ions are not expected to play an important role in the production of surface sulfuric acid. The sulfur ion number flux, which is expected to be an important agent of sulfuric acid production, does peak at the trailing apex, and was found to be correlated to the nonuniform sulfuric acid surface concentration (Figure 9).

Figure 10 displays the relationship between the same measured sulfuric acid concentrations used in Figure 9 and our modeled surface ion energy flux. When the plasma interaction is not considered, a positive correlation is found between sulfuric acid surface concentration and both sulfur ion energy flux ($r = 0.66$, Figure 10a) and total ion energy flux ($r = 0.22$, Figure 10c). The weak correlation between total ion energy flux and sulfuric acid concentration is consistent with the findings of Dalton et al. (2013). Similar to our setup, these authors did not consider any plasma interaction effects. However, when the plasma interaction is taken into account, we find that the measured sulfuric acid concentrations and our modeled ion energy fluxes (of both sulfur alone and all three ion species) are *anti-correlated* (Figures 10b and 10d). Locations where a large amount of energy is deposited by magnetospheric ions have low concentrations of sulfuric acid, and vice versa.

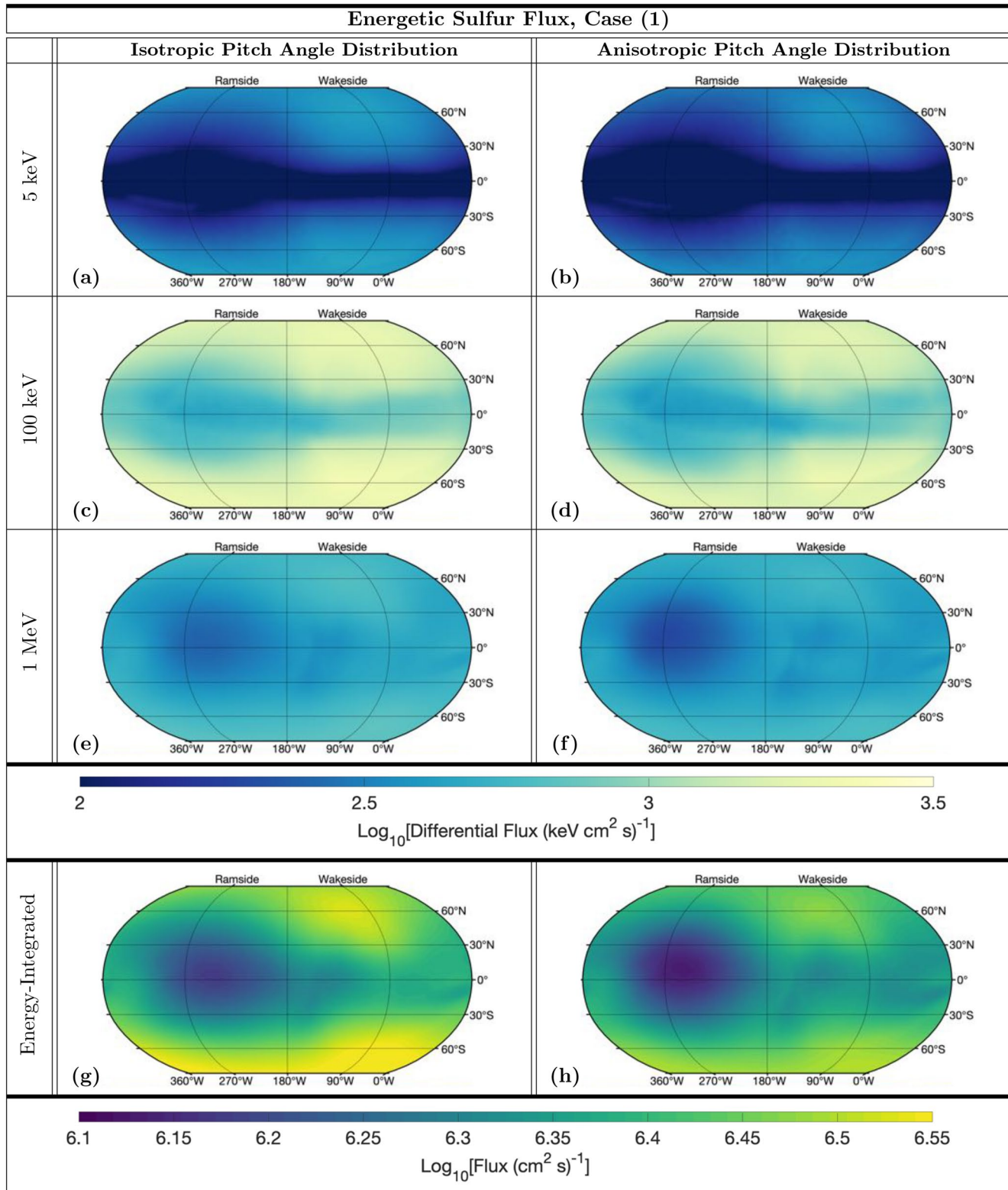


Figure 11. Surface flux of energetic sulfur ions calculated with an isotropic pitch angle distribution (panels (a), (c), (e), and (g)), and a pancake ($\propto \sin(\alpha)$) pitch angle distribution, under the perturbed magnetospheric conditions of case (1). The first three rows contain plots of differential surface flux (in units of $\text{cm}^{-2} \text{ s}^{-1} \text{ keV}^{-1}$) for backtraced ions initialized with energies of 5 keV (panels (a) and (b)), 100 keV (panels (c) and (d)), and 1 MeV (panels (e) and (f)). Number fluxes (in units of $\text{cm}^{-2} \text{ s}^{-1}$) of energetic sulfur ions integrated from 5 keV to 10 MeV are shown in panels (g) and (h).

This anticorrelation between measured sulfuric acid surface concentrations and modeled ion energy fluxes arises from the stark changes to the ion bombardment patterns brought on by the inclusion of the plasma interaction (Figure 8). The surface concentration observed by the NIMS instrument peak near the ramside apex, and decrease longitudinally with distance away from it. When the plasma interaction is *not* considered, the energetic ion flux displays a similar decrease in longitudinal distance from the ramside apex (Figures 8b and 8h), and hence there is a positive correlation between the measured concentrations and the modeled energy flux (Figures 10a and 10c). However, the inclusion of the plasma interaction *reverses* the energetic ion flux pattern near the ramside apex: the intensity of ion bombardment now *increases* with longitudinal distance (Figures 8e and 8h). This reversal caused by the plasma interaction leads to the anticorrelation shown in Figures 10b and 10d. This result suggests that radiolytic processing of the surface by energetic ions is *not* a critical agent for the production of surface sulfuric acid, consistent with the findings of Dalton et al. (2013). However, Cooper et al. (2001) showed that up to 75% of energy deposited onto Europa's surface is carried by electrons, and it is therefore possible that energy deposition by electrons (not ions) is an important agent for sulfuric acid production. However, since significant modifications of our modeling framework would be required to trace the dynamics of magnetospheric electrons (see Section 3.4), we leave modeling of magnetospheric electron surface flux to future work.

In addition to weathering the surface, impacts of magnetospheric ions sputter surface ice, significantly contributing to the generation of Europa's dilute exosphere. Hydrogen sputtered from the surface is largely able to escape Europa's gravity, and as such is the main constituent of the neutral torus along the moon's orbit (e.g., R. E. Johnson et al., 2009; Smith et al., 2019). Molecular oxygen sputtered from the surface is less likely to escape, and therefore is the main constituent of Europa's exosphere (e.g., Hall et al., 1995; Plainaki et al., 2018). To understand the density distribution of Europa's exosphere and its role in forming the neutral torus, it is imperative to have an accurate model of the spatial distribution of magnetospheric ion surface flux. The amount of material sputtered by an incident ion is non-monotonically dependent on a number of parameters, such as the species, charge, velocity, and incidence angles of the ions, as well as the temperature profile of the surface (e.g., R. E. Johnson et al., 2004). Below 1 MeV, the sputtering yields for the ion populations present at Europa's orbit increase monotonically with incident ion energy (Cassidy et al., 2013). Treating Europa's local electromagnetic environment as uniform, Cassidy et al. (2013) found the surface ion flux (and sputtering rate) at Europa to be greatest in the trailing hemisphere and distributed in a bullseye pattern centered around the trailing apex (see Figures 7 and 8 of that work).

When we take into account the plasma interaction, our modeled surface fluxes differ greatly from those of Cassidy et al. (2013), especially for the energetic particles ($E > 5$ keV). In contrast to Cassidy et al. (2013), our model predicts an "inverted" bullseye pattern in energetic ion flux onto Europa's trailing hemisphere, that is, the energetic ion flux *increases* in magnitude with distance from the trailing apex. This "reversal" of the bullseye pattern is caused almost entirely by the draping of the magnetic field lines around Europa, and to a minor degree by gradient drift of energetic ions in the ramside magnetic pileup region. When the plasma interaction is considered, our model also predicts the thermal ion surface flux to be several orders of magnitude lower in the trailing hemisphere, and to be spread more evenly across the surface than suggested by Cassidy et al. (2013). The sputtering yields of incident thermal ions are approximately 100 times less than the sputtering yields of 100 keV ions, and up to 5,000 times less than those of 1 MeV ions (Cassidy et al., 2013; Vorburger & Wurz, 2018). However, the higher flux of the thermal ions may suggest that the thermal population and the energetic population sputter a similar amount of material from the surface.

Therefore, our model suggests that the sputtering rate may be greater at high latitudes, where both the thermal and energetic ion fluxes peak, than previously thought. Furthermore, the sputtering rate in the trailing hemisphere may be significantly less than suggested by Cassidy et al. (2013). We found that the inclusion of the plasma interaction reduces overall magnetospheric ion flux onto many locations on Europa's surface. This finding supports the idea of a "self-limiting" exosphere originally put forward by R. E. Johnson et al. (1982): Ion impacts sputter surface material, building up the exosphere, which in turn generates the Alfvénic field perturbations, thereby protecting the surface from further ion impacts. In this way, a dynamic equilibrium can be reached in Europa's exosphere. However, a rigorous treatment of the sputtering rates requires tabulation of ion incidence angles and inclusion of a full thermal profile of Europa's surface (Cassidy et al., 2013), and is therefore left for future work.

3.5. The Effect of an Anisotropic Pitch Angle Distribution on Energetic Sulfur Flux

Various studies (e.g., Kollmann et al., 2016; Lagg et al., 2003; Mauk et al., 2004) have constrained the PAD of the energetic upstream ions near Europa. Mauk et al. (2004) suggested that the upstream PAD was isotropic to within 25%. However, a recent study by Nénon and André (2019) used Galileo EPD data to show that the PAD of sulfur ions near Europa is nearly sinusoidal, or “pancake-shaped,” with pitch angles near 90° favored over pitch angles near 0° or 180°. To determine the effect of such an anisotropic PAD on our results, in Figure 11, we present modeled flux maps of energetic sulfur ions across Europa’s surface under the perturbed fields of case (1), that is, Europa located near the center of the plasma sheet. The first three rows (panels (a–f)) display the differential surface flux of sulfur ions at select starting energies: 5 keV (panels (a) and (b)), 100 keV (panels (c) and (d)), and 1 MeV (panels (e) and (f)). The final row (panels (g) and (h)) displays the number flux of energetic sulfur ions integrated from 5 keV to 10 MeV using the same discretized starting energies as detailed in Section 2.2. The left column displays flux calculated with an isotropic PAD, while the right column displays flux calculated with a PAD proportional to $\sin(\alpha)$, where α is the pitch angle.

Our results show that such an anisotropic pitch angle distribution, such as the anisotropic distribution of energetic sulfur ions measured by the Galileo EPD instrument (Nénon & André, 2019), has only a subtle effect on sulfur ion flux onto Europa’s surface compared to an isotropic PAD. The slight impact a $\sin(\alpha)$ upstream PAD has on surface flux grows with ion energy. For 5 keV sulfur ions the difference between the flux modeled for an isotropic and an anisotropic PAD is imperceptible (Figures 11a and 11b, respectively). A slight reduction in flux, by a factor of ~ 1.25 compared to the isotropic PAD case, begins to manifest at 100 keV (Figures 11c and 11d), and becomes more prominent at 1 MeV (Figures 11e and 11f). Cassidy et al. (2013) and Breer et al. (2019) showed that at moderate to high energies ($E > 10$ keV), ions with large field-aligned velocities make the major contribution to surface precipitation. Since a $\sin(\alpha)$ PAD contains more particles with large velocities *perpendicular* to the magnetic field (pitch angles close to 90°) than parallel to it (pitch angles close to 0° or 180°), the overall reduction in surface flux due to the anisotropic PAD gradually increases with increasing ion energy. Therefore, the surface flux of the highest energy particles ($E > 500$ keV) undergoes the greatest change when a $\sin(\alpha)$ PAD is utilized instead of an isotropic PAD.

Accordingly, the total number flux of *all* energetic sulfur ions onto Europa’s surface is slightly reduced when an anisotropic PAD is used, while the overall morphology of the influx pattern remains unchanged (Figures 11g and 11h). The integrated flux is lessened by up to 12%, with the greatest change occurring near the poles. Breer et al. (2019) showed that high energy ions ($E > 100$ keV) with large field-aligned velocities preferentially impact near the poles. Therefore, a $\sin(\alpha)$ PAD, which contains fewer of these particles than its isotropic counterpart, results in reduced flux onto Europa’s polar caps.

Overall, the effect of an anisotropic $\sin(\alpha)$ PAD on ion surface flux is small, and does not qualitatively change the total flux pattern. Only the surface flux of the highest energy particles ($E > 1$ MeV) undergoes any discernible change. These high-energy ions are from the tail of the energy distribution $I(E)$, as displayed in Figure 2c. In this tail, the number of upstream ions at a given energy is three to four orders of magnitude lower than near 100 keV. Therefore, the ions which are most affected by the anisotropic PAD only make a very minor contribution to the integrated surface flux. Since an anisotropic PAD does not change the overall sulfur ion flux pattern onto the surface, we judge that the strong correlation between magnetospheric sulfur influx and sulfuric acid concentration would remain largely unchanged if the upstream PAD of energetic sulfur ions is anisotropic.

3.6. The Effect of Exospheric Charge Exchange on Proton Surface Flux

Before magnetospheric particles can impact Europa’s surface, they must pass through the moon’s dilute exosphere. It is possible that upon traversing Europa’s gas envelope, an incident particle will undergo a charge exchange reaction with a neutral exospheric particle. Since such a reaction neutralizes an incident proton before it can reach the surface, exospheric charge exchange may provide additional protection of Europa’s surface from *singly charged* magnetospheric ions. We note that after a charge exchange reaction, the now-neutral hydrogen particle moves along a straight line while (mostly) retaining its original energy. Such an ENA may still precipitate onto the surface and contribute to sputtering.

To investigate the effect of exospheric charge exchange on proton surface flux, we modeled proton trajectories for select starting energies (10, 50, and 100 keV) using the collision model of Birdsall (1991), given in Equation 16, and the H^+ - O_2 charge exchange cross sections provided by Lindsay and Stebbings (2005). Above proton energies of 100 keV, the charge exchange cross sections drop precipitously, and therefore the associated depletion of the impinging proton population is negligible (Basu et al., 1987). Cross-sections are not available in the literature for reactions of multiply charged oxygen and sulfur ions with neutral O_2 , and we therefore restrict this study to energetic protons. Besides, a multiply charged ion will likely not be neutralized on the small length scales of Europa's exosphere (Nénon & André, 2019). Therefore, ion-neutral reactions in Europa's exosphere are not expected to represent a significant loss mechanism for heavy magnetospheric ions with trajectories that carry them into Europa's surface.

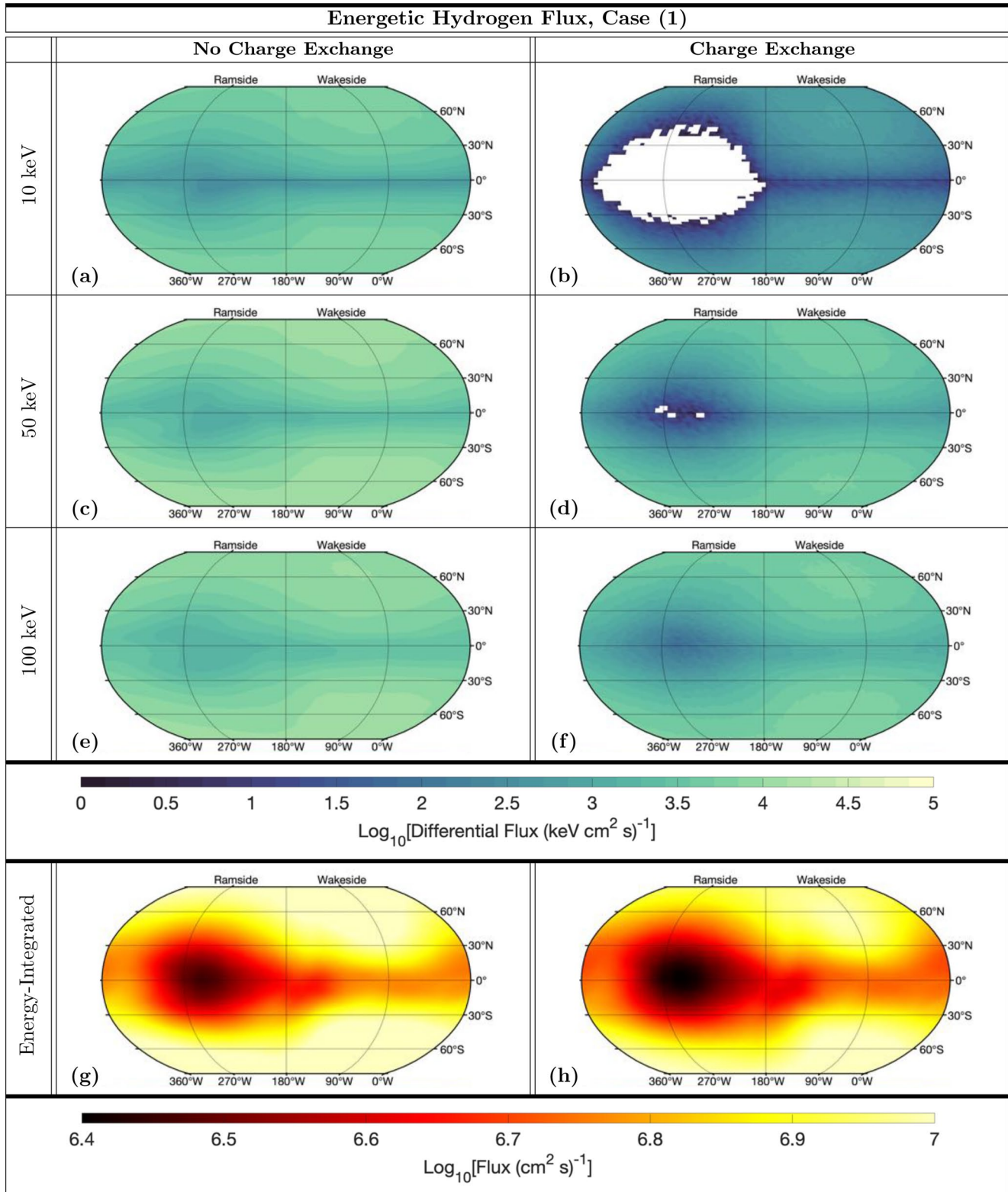
For these model runs we utilized the perturbed field configuration of case (1), that is, Europa is assumed to be located near the center of the plasma sheet. Our results are given in Figure 12. The first three panels in the left column (Figures 12a, 12c, and 12e) display differential surface flux of 10, 50, and 100 keV protons, respectively, *without* the inclusion of charge exchange reactions. The corresponding three panels in the right column (Figures 12b, 12d, and 12f) display differential proton surface flux at 10, 50, and 100 keV starting energies, *with* charge exchange reactions included. The total fluxes of all energetic protons, integrated from 5 keV to 10 MeV without and with charge exchange, are given in Figures 12g and 12h, respectively. For starting energies above 100 keV (where charge exchange reactions become negligible), we again used the flux patterns for protons calculated in Section 3.2 without charge exchange.

Our results show that, overall, the inclusion of charge exchange reduces the energetic proton flux onto Europa's surface. The neutral density of the applied exosphere model (see Equation 4) peaks near Europa's trailing hemisphere apex. Since the efficiency of the charge exchange process grows with increasing neutral density (see Equation 16), the drop in surface flux caused by these reactions is most evident at low latitudes of Europa's trailing hemisphere. The protection of the surface against proton irradiation decreases with energy. For 100 keV protons, the inclusion of charge exchange reactions (Figure 12f) reduces differential surface flux only by a factor of 3 compared to the setup without charge exchange (Figure 12e). At the initial proton energy of 50 keV (Figures 12c and 12d), the protection grows to a factor of 5 at most surface locations. When the starting energy is dropped further to 10 keV (see Figures 12a and 12b), proton depletion via charge exchange forms a large, quasi-elliptical region of nearly zero flux around the trailing apex. Everywhere else, flux is reduced across the surface by up to two orders of magnitude compared to the case without charge exchange. However, while charge exchange reactions lessen the *magnitude* of the proton surface flux, the overall *shape* of the influx pattern is not drastically altered.

The decreasing efficiency of charge exchange reactions with growing ion energy can be explained through Equation 16, which gives the reaction probability as $P = 1 - \exp(-n_n \sigma v' |dt|)$. As the magnitude of $n_n \sigma(E) v' |dt|$ grows, the probability of charge exchange rises. For a given neutral density and path length $dl = v' |dt|$ traveled by an ion, the probability of charge exchange is determined by the collisional cross-section σ . Since σ drops by an order of magnitude over the ion energy range from 10 to 100 keV (Lindsay & Stebbings, 2005), the depletion of the energetic proton population by exospheric charge exchange correspondingly decreases.

Overall, charge exchange with neutral oxygen provides additional protection of the surface against energetic proton impacts at energies below 100 keV. The total surface flux of all energetic protons (Figures 12g and 12h) is reduced by a factor of 2–3, with the greatest reduction occurring near the trailing hemisphere apex. Charge exchange reactions therefore enhance the reduction of energetic proton surface flux onto the trailing hemisphere that our model already revealed without charge exchange. Additionally, these findings further corroborate the notion of a self-limiting atmosphere suggested by R. E. Johnson et al. (1982). Sputtered neutrals create a ram-wake asymmetry in the atmosphere which, through the Alfvénic interaction and exospheric charge exchange, partially protects the trailing hemisphere from further irradiation and sputtering. However, we emphasize that the ENAs generated during charge exchange reactions can still impact the surface and contribute to sputtering. We leave the treatment of such energetic neutrals to future work.

We did not yet take into account charge exchange reactions between Europa's exosphere and the upstream *thermal* proton population. In contrast to the energetic ions, charge exchange reactions of the thermal protons would also affect the currents in the Alfvén wings and electromagnetic fields (Neubauer, 1998).



Therefore this process would have to be included in the AIKEF simulations as well. However, this would require the separation of the upstream plasma in AIKEF into its three constituents (hydrogen, oxygen, and sulfur). The high number of macroparticles required to accurately represent the upstream distribution of *each* of these three species would drastically increase the computational time of the AIKEF simulations. Furthermore, collision cross-sections of neutral O₂ with sulfur ions are not available in the literature for any energy, making such a comprehensive treatment of these effects currently infeasible. Therefore, we leave the calculation of thermal ion surface flux with the inclusion of charge exchange to future work.

4. Summary and Concluding Remarks

In this study, we have presented the first model of magnetospheric ion flux onto the surface of Europa that considers the time-varying, perturbed electromagnetic fields near the moon. Our intention was to determine how these field perturbations modify ion surface flux, compared to less complex field configurations that include only the Jovian background field and Europa's induced dipole. To accomplish this, we have combined the electromagnetic fields from an established hybrid model (Arnold et al., 2019) with an expanded version of the GENTOO particle-tracing tool (Liuzzo et al., 2019b) to calculate spatially resolved maps of thermal and energetic hydrogen, oxygen, and sulfur ion flux onto Europa's surface. We considered the ambient magnetospheric conditions and associated field perturbations near Europa at three locations relative to the center of the Jovian plasma sheet: (1) near the *center* of the sheet, (2) far *north* of the center of the sheet, and (3) far *south* of the center of the sheet. We utilized in-situ particle data from the Galileo spacecraft to calculate the contribution of different ion species and energies to surface flux. These results were combined to determine the averaged surface irradiation by magnetospheric ions for an *entire* synodic rotation. We also identified correlations between the modeled surface flux patterns and the spatial variability of sulfuric acid concentrations observed across Europa's surface. To constrain the robustness of our results, we modeled the effect of an anisotropic upstream PAD and exospheric charge exchange on the energetic ion influx patterns. Overall, our study aims to bridge the gap between a rigorous treatment of Europa's electromagnetic environment and a detailed understanding of its surface properties.

Our major findings can be summarized as follows:

1. The sub-alfvénic interaction of the upstream thermal plasma with Europa's ionosphere and induced dipole drastically alters ion surface flux patterns, compared to those obtained for uniform fields in preceding studies (Cassidy et al., 2013). Draping of the magnetospheric field lines around the moon allows thermal ions ($E < 5$ keV) from the upstream distribution to impinge onto *every* location on Europa's surface. Whereas a setup that considers only the Jovian magnetospheric field and Europa's induced dipole suggests that the leading hemisphere receives *zero* thermal ion flux, a model that includes the plasma interaction reveals that the leading hemisphere is exposed to significant levels of irradiation by thermal ions
2. Due to the high thermal velocity of the incident thermal ion flow, thermal ions with velocities far from the peak of the upstream Maxwellian distribution make a significant contribution to surface flux. This contribution is strongest for hydrogen, which features the largest thermal velocity of the three species considered. Therefore, a kinetic treatment of the thermal upstream ions is required to accurately model their surface flux patterns
3. The inclusion of the draped field lines at Europa redistributes energetic ($E > 5$ keV) ion surface flux, compared to when only the Jovian background field and Europa's induced dipole are considered. Energetic ions traveling along draped field lines near the moon must pass a larger distance within one gyroradius of the surface than without field line draping. This causes the energetic ion population to be depleted at high European latitudes before reaching the trailing hemisphere apex. This depletion of energetic ions at high latitudes results in an "inverted" bullseye pattern of the energetic ion surface flux.

Figure 12. Maps of energetic proton flux onto Europa's surface at select energies calculated with the perturbed magnetospheric conditions of case (1). Panels (a) and (b) display the differential flux of 10 keV protons, panels (c) and (d) display the differential flux of 50 keV protons, and panels (e) and (f) display the differential flux of 100 keV protons onto the surface. The left column (panels (a), (c), and (e)) displays surface flux *without* the inclusion of charge exchange reactions, while the right column (panels (b), (d), and (f)) displays surface flux *with* the inclusion of charge exchange reactions. Similar to Figures 4, 6, and 7, white areas denote surface regions that receive differential flux less than 10^0 keV⁻¹ cm⁻² s⁻¹. Total number flux of energetic protons integrated across the energy range from 5 keV to 10 MeV is shown in panels (g) and (h).

- Energetic ion flux is minimized at the trailing hemisphere apex and increases with distance away from it. This is in contrast to energetic ion surface flux obtained by a setup that does not include plasma currents
4. Despite the drastic alterations of ion surface flux patterns imposed by the field perturbations, a strong correlation still exists between measured surface concentrations of sulfuric acid and influx of magnetospheric sulfur ions. These results support the notion that much of the sulfur bound in the observed deposits of sulfuric acid on Europa's surface (Dalton et al., 2013) is exogenic in origin (i.e., originating from the moon's space environment). However, our study has not taken into account the surface flux of magnetospheric electrons, which Dalton et al. (2013) hypothesized plays a significant role in "preparing" the surface for sulfur ion implantation. The role of magnetospheric electron surface flux in combination with ion flux will be explored in future work
 5. Changing from an isotropic PAD to a pancake ($\propto \sin(\alpha)$) distribution does not significantly affect the spatial distribution of energetic sulfur ion flux onto Europa's surface, nor the proposed correlation to observed sulfuric acid concentrations. Assuming a $\sin(\alpha)$ PAD slightly reduces the flux of high energy particles ($E > 500$ keV) onto Europa's surface, with the greatest change occurring near the poles. However, at these energies the energy distribution $I(E)$ of the ions is only sparsely populated, making the contribution of this anisotropy in the PAD to the total surface flux negligible
 6. Charge exchange reactions in Europa's asymmetric exosphere further protect the trailing hemisphere from energetic proton bombardment. However, after having been neutralized, these hydrogen atoms maintain their initial energy and continue along ballistic trajectories. Therefore, they may still contribute to surface erosion and sputtering

A complete analysis of surface-plasma interactions at Europa requires analysis of the behavior of electrons in the perturbed electromagnetic fields, in addition to ions. However, the study of electron dynamics near the moon is more complex than that of ions. The high field-aligned velocities of energetic electrons allow them to leave Europa's interaction environment, travel to the polar ionosphere of Jupiter, be mirrored back and re-intercept Europa (Paranicas et al., 2009). As such, electrons may make multiple attempts to impact Europa's surface, and their treatment requires coupling of the local AIKEF model of Europa's interaction to a global model of Jupiter's magnetosphere (Liuzzo et al., 2019a, 2020). Furthermore, electrons in the energy range studied here require a relativistic treatment: the (then nonlinear) equations of motion can no longer be solved using, for example, a Runge-Kutta scheme. Instead, the technique of Vay (2008) needs to be implemented. Calculation of electron surface flux near Europa therefore represents a significant modification of the model implemented here, and we therefore leave such analysis to future work. A more detailed analysis of the effects of magnetospheric ion surface flux on surface chemistry and generation of Europa's dilute exosphere will be the subject of a follow-up publication.

Data Availability Statement

Results from both the AIKEF hybrid model and the GENTOO particle-tracing model can be downloaded from <http://doi.org/10.5281/zenodo.4313883>.

Acknowledgments

The authors are grateful to the NASA Solar System Workings 2018 Program (Grant no. # 80NSSC20K0463) for financial support. The authors would also like to thank both referees for careful inspection of the manuscript and for valuable comments.

References

- Arnold, H., Liuzzo, L., & Simon, S. (2019). Magnetic signatures of a plume at Europa during the Galileo E26 flyby. *Geophysical Research Letters*, 46(3), 1149–1157. <https://doi.org/10.1029/2018GL081544>
- Arnold, H., Liuzzo, L., & Simon, S. (2020). Plasma interaction signatures of plumes at Europa. *Journal of Geophysical Research: Space Physics*, 125(1), e2019JA027346. <https://doi.org/10.1029/2019JA027346>
- Arnold, H., Simon, S., & Liuzzo, L. (2020). Applying ion energy spectrograms to search for plumes at Europa. *Journal of Geophysical Research: Space Physics*, 125, e2020JA028376. <https://doi.org/10.1029/2020JA028376>
- Bagenal, F., & Delamere, P. A. (2011). Flow of mass and energy in the magnetospheres of Jupiter and Saturn. *Journal of Geophysical Research*, 116, A05209. <https://doi.org/10.1029/2010JA016294>
- Bagenal, F., Sidrow, E., Wilson, R. J., Cassidy, T. A., Dols, V., Cray, F. J., et al. (2015). Plasma conditions at Europa's orbit. *Icarus*, 261, 1–13. <https://doi.org/10.1016/j.icarus.2015.07.036>
- Basu, B., Jasperse, J. R., Robinson, R. M., Vondrak, R. R., & Evans, D. S. (1987). Linear transport theory of auroral proton precipitation: A comparison with observations. *Journal of Geophysical Research*, 92(A6), 5920–5932. <https://doi.org/10.1029/ja092ia06p05920>
- Birdsall, C. K. (1991). Particle-in-cell charged-particle simulations, plus Monte Carlo collisions with neutral atoms, PIC-MCC. *IEEE Transactions on Plasma Science*, 19(2), 65–85. <https://doi.org/10.1109/27.106800>
- Blöcker, A., Saur, J., & Roth, L. (2016). Europa's plasma interaction with an inhomogeneous atmosphere: Development of Alfvén winglets within the Alfvén wings. *Journal of Geophysical Research: Space Physics*, 121(10), 9794–9828. <https://doi.org/10.1002/2016ja022479>

- Bonfond, B., Saur, J., Grodent, D., Badman, S. V., Bisikalo, D., Shematovich, V., et al. (2017). The tails of the satellite auroral footprints at Jupiter. *Journal of Geophysical Research: Space Physics*, 122(8), 7985–7996. <https://doi.org/10.1002/2017ja024370>
- Breer, B. R., Liuzzo, L., Arnold, H., Andersson, P. N., & Simon, S. (2019). Energetic ion dynamics in the perturbed electromagnetic fields near Europa. *Journal of Geophysical Research: Space Physics*, 124, 7592, 7613. <https://doi.org/10.1029/2019JA027147>
- Carlson, R. W., Anderson, M. S., Mehlman, R., & Johnson, R. E. (2005). Distribution of hydrate on Europa: Further evidence for sulfuric acid hydrate. *Icarus*, 177(2), 461–471. <https://doi.org/10.1016/j.icarus.2005.03.026>
- Carlson, R. W., Johnson, R. E., & Anderson, M. S. (1999). Sulfuric acid on Europa and the radiolytic sulfur cycle. *Science*, 286(5437), 97–99. <https://doi.org/10.1126/science.286.5437.97>
- Carlson, R. W., Weissman, P. R., Weissman, P. R., & Smythe, W. D., Mahoney, J. C. (1992). Near-infrared mapping spectrometer experiment on Galileo. *Space Science Reviews*, 60(1–4), 457–502. https://doi.org/10.1007/BF0021686510.1007/978-94-011-2512-3_18
- Cassidy, T. A., Paranicas, C. P., Shirley, J. H., Dalton, III, J. B., Teolis, B. D., Johnson, R. E., et al. (2013). Magnetospheric ion sputtering and water ice grain size at Europa. *Planetary and Space Science*, 77, 64–73. <https://doi.org/10.1016/j.pss.2012.07.008>
- Clark, G., Mauk, B. H., Kollmann, P., Paranicas, C., Bagenal, F., Allen, R. C., et al. (2020). Heavy ion charge states in Jupiter's polar magnetosphere inferred from auroral megavolt electric potentials. *Journal of Geophysical Research: Space Physics*, 125, e2020JA028052. <https://doi.org/10.1029/2020JA028052>
- Clark, G., Mauk, B. H., Paranicas, C., Kollmann, P., & Smith, H. T. (2016). Charge states of energetic oxygen and sulfur ions in Jupiter's magnetosphere. *Journal of Geophysical Research: Space Physics*, 121(3), 2264–2273. <https://doi.org/10.1002/2015ja022257>
- Connerney, J. E. P., Acuña, M. H., & Ness, N. F. (1981). Modeling the Jovian current sheet and inner magnetosphere. *Journal of Geophysical Research*, 86(A10), 8370–8384. <https://doi.org/10.1029/ja086ia10p08370>
- Connerney, J. E. P., Kotsiaros, S., Oliverson, R. J., Espley, J. R., Joergensen, J. L., Joergensen, P. S., et al. (2018). A new model of Jupiter's magnetic field from Juno's first nine orbits. *Geophysical Research Letters*, 45(6), 2590–2596. <https://doi.org/10.1002/2018gl077312>
- Connerney, J. E. P., Timmins, S., Hecceg, M., & Joergensen, J. L. (2020). A Jovian magnetodisc model for the Juno era. *Journal of Geophysical Research: Space Physics*, 125(10), e2020JA028138. <https://doi.org/10.1029/2020JA028138>
- Cooper, J., Johnson, R. E., Mauk, B. H., Garrett, H. B., & Gehrels, N. (2001). Energetic ion and electron irradiation of the icy Galilean satellites. *Icarus*, 149(1), 133–159. <https://doi.org/10.1006/icar.2000.6498>
- Dalton, J. B., Cassidy, T., Paranicas, C., Shirley, J. H., Prockter, L. M., & Kamp, L. W. (2013). Exogenic controls on sulfuric acid hydrate production at the surface of Europa. *Planetary and Space Science*, 77, 45–63. <https://doi.org/10.1016/j.pss.2012.05.013>
- Dalton, J. B., Shirley, J. H., & Kamp, L. W. (2012). Europa's icy bright plains and dark linea: Exogenic and endogenic contributions to composition and surface properties. *Journal of Geophysical Research*, 117(E3). <https://doi.org/10.1029/2011JE003909>
- Desai, R. T., Cowee, M. M., Wei, H., Fu, X., Gary, S. P., Volwerk, M., & Coates, A. J. (2017). Hybrid simulations of positively and negatively charged pickup ions and cyclotron wave generation at Europa. *Journal of Geophysical Research: Space Physics*, 122(10), 408–410. <https://doi.org/10.1002/2017JA024479>
- Doggett, T., Greeley, R., Figueredo, P., & Tanaka, K. (2009). Geologic stratigraphy and evolution of Europa's surface. In R. T. Pappalardo, W. B. McKinnon, & K. K. Khurana, (Eds.), *Europa* (p. 137). University of Arizona Press.
- Famá, M., Shi, J., & Baragiola, R. A. (2008). Sputtering of ice by low-energy ions. *Surface Science*, 602(1), 156–161. <https://doi.org/10.1016/j.susc.2007.10.002>
- Fatemi, S., Poppe, A. R., Khurana, K. K., Holmström, M., & Delory, G. T. (2016). On the formation of Ganymede's surface brightness asymmetries: Kinetic simulations of Ganymede's magnetosphere. *Geophysical Research Letters*, 43(10), 4745–4754. <https://doi.org/10.1002/2016gl068363>
- Geiss, J., Gloeckler, G., Balsiger, H., Fisk, L. A., Galvin, A. B., Gliem, F., et al. (1992). Plasma composition in Jupiter's magnetosphere: Initial results from the solar wind ion composition spectrometer. *Science*, 257(5076), 1535–1539. <https://doi.org/10.1126/science.257.5076.1535>
- Hall, D. T., Strobel, D. F., Feldman, P. D., McGrath, M. A., & Weaver, H. A. (1995). Detection of an oxygen atmosphere on Jupiter's moon Europa. *Nature*, 373(6516), 677–679. <https://doi.org/10.1038/373677a0>
- Hendrix, A. R., Cassidy, T. A., Johnson, R. E., Paranicas, C., & Carlson, R. W. (2011). Europa's disk-resolved ultraviolet spectra: Relationships with plasma flux and surface terrains. *Icarus*, 212(2), 736–743. <https://doi.org/10.1016/j.icarus.2011.01.023>
- Hill, T. W., & Michel, F. C. (1976). Heavy ions from the Galilean satellites and the centrifugal distortion of the Jovian magnetosphere. *Journal of Geophysical Research*, 81(25), 4561–4565. <https://doi.org/10.1029/ja081i025p04561>
- Huybrighs, H. L. F., Roussos, E., Blöcker, A., Krupp, N., Futaana, Y., Barabash, S., et al. (2020). An active plume eruption on Europa during Galileo flyby E26 as indicated by energetic proton depletions. *Geophysical Research Letters*, 47(10), e2020GL087806. <https://doi.org/10.1029/2020GL087806>
- Ip, W.-H., Williams, D. J., McEntire, R. W., & Mauk, B. H. (1998). Ion sputtering and surface erosion at Europa. *Geophysical Research Letters*, 25(6), 829–832. <https://doi.org/10.1029/98gl00472>
- Jia, X., Kivelson, M. G., Khurana, K. K., & Kurth, W. S. (2018). Evidence of a plume on Europa from Galileo magnetic and plasma wave signatures. *Nature Astronomy*, 2(6), 459–464. <https://doi.org/10.1038/s41550-018-0450-z>
- Johnson, R. E., Burger, M. H., Cassidy, T. A., Leblanc, F., Marconi, M., & Smyth, W. H. (2009). Composition and detection of Europa's sputter-induced atmosphere. In R. T. Pappalardo, W. B. McKinnon, & K. K. Khurana, (Eds.), *Europa* (p. 507). University of Arizona Press.
- Johnson, R. E., Carlson, R. W., Cooper, J. F., Paranicas, C., Moore, M. H., & Wong, M. C. (2004). Radiation effects on the surfaces of the Galilean satellites. In F. Bagenal, T. E. Dowling, & W. B. McKinnon, (Eds.), *Jupiter: The planet, satellites and magnetosphere* (Vol. 1, pp. 485–512). Cambridge University Press.
- Johnson, R. E., Lanzerotti, L. J., & Brown, W. L. (1982). Planetary applications of ion induced erosion of condensed-gas frosts. *Nuclear Instruments and Methods in Physics Research*, 198, 147–157. [https://doi.org/10.1016/0167-5087\(82\)90066-7](https://doi.org/10.1016/0167-5087(82)90066-7)
- Johnson, T. V., Soderblom, L. A., Mosher, J. A., Danielson, G. E., Cook, A. F., & Kupferman, P. (1983). Global multispectral mosaics of the icy Galilean satellites. *Journal of Geophysical Research*, 88(B7), 5789–5805. <https://doi.org/10.1029/jb088ib07p05789>
- Joy, S. P., Kivelson, M. G., Walker, R. J., Khurana, K. K., Russell, C. T., & Ogino, T. (2002). Probabilistic models of the Jovian magnetopause and bow shock locations. *Journal of Geophysical Research*, 107, 1309. <https://doi.org/10.1029/2001JA009146>
- Khurana, K. K. (1997). Euler potential models of Jupiter's magnetospheric field. *Journal of Geophysical Research*, 102, 11295–11306. <https://doi.org/10.1029/97JA00563>
- Khurana, K. K., & Kivelson, M. G. (1993). Inference of the angular velocity of plasma in the Jovian magnetosphere from the sweepback of magnetic field. *Journal of Geophysical Research*, 98(A1), 67–79. <https://doi.org/10.1029/92ja01890>
- Khurana, K. K., Kivelson, M. G., Stevenson, D. J., Schubert, G., Russell, C. T., Walker, R. J., & Polanskey, C. (1998). Induced magnetic fields as evidence for subsurface oceans in Europa and Callisto. *Nature*, 395(6704), 777–780. <https://doi.org/10.1038/27394>

- Kim, T. K., Ebert, R. W., Valek, P. W., Allegrini, F., McComas, D. J., Bagenal, F., et al. (2020). Survey of ion properties in Jupiter's plasma sheet: Juno JADE-I observations. *Journal of Geophysical Research: Space Physics*, *125*(4), e2019JA027696. <https://doi.org/10.1029/2019JA027696>
- Kivelson, M. G., Bagenal, F., Kurth, W. S., Neubauer, F. M., Paranicas, C., & Saur, J. (2004). Magnetospheric interactions with satellites. In F. Bagenal, T. E. Dowling & W. B. McKinnon (Eds.), *Jupiter: The planet, satellites and magnetosphere* (pp. 513–536). Cambridge University Press.
- Kivelson, M. G., Khurana, K. K., Russell, C. T., Volwerk, M., Walker, R. J., & Zimmer, C. (2000). Galileo magnetometer measurements: A stronger case for a subsurface ocean at Europa. *Science*, *289*(5483), 1340–1343. <https://doi.org/10.1126/science.289.5483.1340>
- Kivelson, M. G., Khurana, K. K., Stevenson, D. J., Bennett, L., Joy, S., Russell, C. T., et al. (1999). Europa and Callisto: Induced or intrinsic fields in a periodically varying plasma environment. *Journal of Geophysical Research*, *104*(A3), 4609–4625. <https://doi.org/10.1029/1998JA900095>
- Kivelson, M. G., Khurana, K. K., & Volwerk, M. (2009). Europa's Interaction with the Jovian Magnetosphere. In R. T. Pappalardo, W. B. McKinnon, & K. K. Khurana (Eds.), *Europa* (p. 545).
- Kollmann, P., Hill, M. E., McNutt, R. L., Allen, R. C., Clark, G., Andrews, B., et al. (2019). Suprathermal ions in the outer heliosphere. *Acta Pathologica Japonica*, *87*(1), 46. <https://doi.org/10.3847/1538-4357/ab125f>
- Kollmann, P., Paranicas, C., Clark, G., Roussos, E., Lagg, A., & Krupp, N. (2016). The vertical thickness of Jupiter's Europa gas torus from charged particle measurements. *Geophysical Research Letters*, *43*(18), 9425–9433. <https://doi.org/10.1002/2016gl070326>
- Kurth, W. S., Gurnett, D. A., Persoon, A. M., Roux, A., Bolton, S. J., & Alexander, C. J. (2001). The plasma wave environment of Europa. *Planetary and Space Science*, *49*(3), 345–363. [https://doi.org/10.1016/S0032-0633\(00\)00156-2](https://doi.org/10.1016/S0032-0633(00)00156-2)
- Lagg, A., Krupp, N., Woch, J., & Williams, D. J. (2003). In-situ observations of a neutral gas torus at Europa. *Geophysical Research Letters*, *30*(11). <https://doi.org/10.1029/2003gl017214>
- Lindsay, B. G., & Stebbings, R. F. (2005). Charge transfer cross sections for energetic neutral atom data analysis. *Journal of Geophysical Research*, *110*(A12). <https://doi.org/10.1029/2005ja011298>
- Liuzzo, L., Feyerabend, M., Simon, S., & Motschmann, U. (2015). The impact of Callisto's atmosphere on its plasma interaction with the Jovian magnetosphere. *Journal of Geophysical Research: Space Physics*, *120*(11), 9401–9427. <https://doi.org/10.1002/2015ja021792>
- Liuzzo, L., Poppe, A. R., Paranicas, C., N n n, Q., Fatemi, S., & Simon, S. (2020). Variability in the energetic electron bombardment of Ganymede. *Journal of Geophysical Research: Space Physics*, *125*, e2020JA028347. <https://doi.org/10.1029/2020JA028347>
- Liuzzo, L., Simon, S., & Feyerabend, M. (2018). Observability of Callisto's inductive signature during the Jupiter Icy Moons Explorer Mission. *Journal of Geophysical Research: Space Physics*, *123*(11), 9045–9054. <https://doi.org/10.1029/2018ja025951>
- Liuzzo, L., Simon, S., Feyerabend, M., & Motschmann, U. (2016). Disentangling plasma interaction and induction signatures at Callisto: The Galileo C10 flyby. *Journal of Geophysical Research: Space Physics*, *121*(9), 8677–8694. <https://doi.org/10.1002/2016ja023236>
- Liuzzo, L., Simon, S., Feyerabend, M., & Motschmann, U. (2017). Magnetic signatures of plasma interaction and induction at Callisto: The Galileo C21, C22, C23, and C30 flybys. *Journal of Geophysical Research: Space Physics*, *122*(7), 7364–7386. <https://doi.org/10.1002/2017ja024303>
- Liuzzo, L., Simon, S., & Regoli, L. (2019a). Energetic electron dynamics near Callisto. *Planetary and Space Science*, *179*, 104726. <https://doi.org/10.1016/j.pss.2019.104726>
- Liuzzo, L., Simon, S., & Regoli, L. (2019b). Energetic ion dynamics near Callisto. *Planetary and Space Science*, *166*, 23–53. <https://doi.org/10.1016/j.pss.2018.07.014>
- Mauk, B. H., Clark, G., Allegrini, F., Bagenal, F., Bolton, S. J., Connerney, J. E. P., et al. (2020). Juno energetic neutral atom (ENA) remote measurements of magnetospheric injection dynamics in Jupiter's Io torus regions. *Journal of Geophysical Research: Space Physics*, *125*(5), e2020JA027964. <https://doi.org/10.1029/2020JA027964>
- Mauk, B. H., Mitchell, D. G., McEntire, R. W., Paranicas, C. P., Roelof, E. C., Williams, D. J., et al. (2004). Energetic ion characteristics and neutral gas interactions in Jupiter's magnetosphere. *Journal of Geophysical Research*, *109*(A9). <https://doi.org/10.1029/2003ja010270>
- McEwen, A. S. (1986). Exogenic and endogenic albedo and color patterns on Europa. *Journal of Geophysical Research*, *91*(B8), 8077–8097. <https://doi.org/10.1029/JB091iB08p08077>
- M ller, J., Simon, S., Motschmann, U., Sch le, J., Glassmeier, K.-H., & Pringle, G. J. (2011). A.I.K.E.F: Adaptive hybrid model for space plasma simulations. *Computer Physics Communications*, *182*(4), 946–966. <https://doi.org/10.1016/j.cpc.2010.12.033>
- N n n, Q., & Andr , N. (2019). Evidence of Europa neutral gas torii from energetic sulfur ion measurements. *Geophysical Research Letters*, *46*(7), 3599–3606. <https://doi.org/10.1029/2019gl082200>
- N n n, Q., Sicard, A., Kollmann, P., Garrett, H. B., Sauer, S. P. A., & Paranicas, C. (2018). A physical model of the proton radiation belts of Jupiter inside Europa's orbit. *Journal of Geophysical Research: Space Physics*, *123*(5), 3512–3532. <https://doi.org/10.1029/2018ja025216>
- Neubauer, F. M. (1980). Nonlinear standing Alfv n wave current system at Io: Theory. *Journal of Geophysical Research*, *85*, 1171–1178. <https://doi.org/10.1029/JA085iA03p01171>
- Neubauer, F. M. (1998). The sub-Alfv nic interaction of the Galilean satellites with the Jovian magnetosphere. *Journal of Geophysical Research*, *103*, 19843–19866. <https://doi.org/10.1029/97JE03370>
- Neubauer, F. M. (1999). Alfv n wings and electromagnetic induction in the interiors: Europa and Callisto. *Journal of Geophysical Research*, *104*, 28671–28684. <https://doi.org/10.1029/1999JA900217>
- Paranicas, C., Carlson, R. W., & Johnson, R. E. (2001). Electron bombardment of Europa. *Geophysical Research Letters*, *28*(4), 673–676. <https://doi.org/10.1029/2000gl012320>
- Paranicas, C., Cooper, J. F., Garrett, H. B., Johnson, R. E., & Sturmer, S. J. (2009). Europa's radiation environment and its effects on the surface. In R. T. Pappalardo, W. B. McKinnon, & K. K. Khurana (Eds.), *Europa* (p. 529). University of Arizona Press.
- Paranicas, C., McEntire, R. W., Cheng, A. F., Lagg, A., & Williams, D. J. (2000). Energetic charged particles near Europa. *Journal of Geophysical Research*, *105*(A7), 16005–16015. <https://doi.org/10.1029/1999ja000350>
- Paranicas, C., Ratliff, J. M., Mauk, B. H., Cohen, C., & Johnson, R. E. (2002). The ion environment near Europa and its role in surface energetics. *Geophysical Research Letters*, *29*(5), 18–21. <https://doi.org/10.1029/2001gl014127>
- Paterson, W. R., Frank, L. A., & Ackerson, K. L. (1999). Galileo plasma observations at Europa: Ion energy spectra and moments. *Journal of Geophysical Research*, *104*(A10), 22779–22791. <https://doi.org/10.1029/1999ja900191>
- Patterson, G. W., Paranicas, C., & Prockter, L. M. (2012). Characterizing electron bombardment of Europa's surface by location and depth. *Icarus*, *220*(1), 286–290. <https://doi.org/10.1016/j.icarus.2012.04.024>
- Plainaki, C., Cassidy, T. A., Shematovich, V. I., Milillo, A., Wurz, P., Vorburger, A., et al. (2018). Towards a global unified model of Europa's tenuous atmosphere. *Space Science Reviews*, *214*(1), 40. <https://doi.org/10.1007/s11214-018-0469-6>

- Plainaki, C., Milillo, A., Massetti, S., Mura, A., Jia, X., Orsini, S., et al. (2015). The H₂O and O₂ exospheres of Ganymede: The result of a complex interaction between the Jovian magnetospheric ions and the icy moon. *Icarus*, *245*, 306–319. <https://doi.org/10.1016/j.icarus.2014.09.018>
- Plainaki, C., Milillo, A., Mura, A., Orsini, S., Massetti, S., & Cassidy, T. (2012). The role of sputtering and radiolysis in the generation of Europa exosphere. *Icarus*, *218*, 956–966. <https://doi.org/10.1016/j.icarus.2012.01.023>
- Plainaki, C., Milillo, A., Mura, A., Saur, J., Orsini, S., & Massetti, S. (2013). Exospheric O₂ densities at Europa during different orbital phases. *Planetary and Space Science*, *88*, 42–52. <https://doi.org/10.1016/j.pss.2013.08.011>
- Poppe, A. R., Fatemi, S., & Khurana, K. K. (2018). Thermal and energetic ion dynamics in Ganymede's magnetosphere. *Journal of Geophysical Research: Space Physics*, *123*(6), 4614–4637. <https://doi.org/10.1029/2018ja025312>
- Pospieszalska, M. K., & Johnson, R. E. (1989). Magnetospheric ion bombardment profiles of satellites: Europa and Dione. *Icarus*, *78*(1), 1–13. [https://doi.org/10.1016/0019-1035\(89\)90065-1](https://doi.org/10.1016/0019-1035(89)90065-1)
- Roth, L., Retherford, K. D., Saur, J., Strobel, D. F., Feldman, P. D., McGrath, M. A., & Nimmo, F. (2014). Orbital apocenter is not a sufficient condition for HST/STIS detection of Europa's water vapor aurora. *Proceedings of the National Academy of Sciences of the United States of America*, *111*(48), E5123–E5132. <https://doi.org/10.1073/pnas.1416671111>
- Rubin, M., Jia, X., Altwegg, K., Combi, M. R., Daldorff, L. K. S., Gombosi, T. I., et al. (2015). Self-consistent multifluid MHD simulations of Europa's exospheric interaction with Jupiter's magnetosphere. *Journal of Geophysical Research: Space Physics*, *120*(5), 3503–3524. <https://doi.org/10.1002/2015ja021149>
- Saur, J., Feldman, P. D., Roth, L., Nimmo, F., Strobel, D. F., Retherford, K. D., et al. (2011). Hubble space telescope/advanced camera for surveys observations of Europa's atmospheric ultraviolet emission at eastern elongation. *The Astrophysical Journal*, *738*, 153. <https://doi.org/10.1088/0004-637X/738/2/153>
- Saur, J., Neubauer, F. M., & Glassmeier, K.-H. (2010). Induced magnetic fields in solar system bodies. *Space Science Reviews*, *152*(1–4), 391–421. <https://doi.org/10.1007/s11214-009-9581-y>
- Saur, J., Strobel, D. F., & Neubauer, F. M. (1998). Interaction of the Jovian magnetosphere with Europa: Constraints on the neutral atmosphere. *Journal of Geophysical Research*, *103*(E9), 19947–19962. <https://doi.org/10.1029/97je03556>
- Schilling, N., Neubauer, F. M., & Saur, J. (2007). Time-varying interaction of Europa with the Jovian magnetosphere: Constraints on the conductivity of Europa's subsurface ocean. *Icarus*, *192*(1), 41–55. <https://doi.org/10.1016/j.icarus.2007.06.024>
- Šebek, O., Trávníček, P. M., Walker, R. J., & Hellinger, P. (2016). Ion cyclotron instability at Io: Hybrid simulation results compared to in situ observations. *Journal of Geophysical Research: Space Physics*, *121*, 7514–7534. <https://doi.org/10.1002/2016JA022477>
- Seufert, M., Saur, J., & Neubauer, F. M. (2011). Multi-frequency electromagnetic sounding of the Galilean moons. *Icarus*, *214*(2), 477–494. <https://doi.org/10.1016/j.icarus.2011.03.017>
- Shirley, J. H., Dalton, J. B., Prockter, L. M., & Kamp, L. W. (2010). Europa's ridged plains and smooth low albedo plains: Distinctive compositions and compositional gradients at the leading side-trailing side boundary. *Icarus*, *210*(1), 358–384. <https://doi.org/10.1016/j.icarus.2010.06.018>
- Shprits, Y. Y., Menietti, J. D., Drozdov, A. Y., Horne, R. B., Woodfield, E. E., Groene, J. B., et al. (2018). Strong whistler mode waves observed in the vicinity of Jupiter's moons. *Nature Communications*, *9*(1). <https://doi.org/10.1038/s41467-018-05431-x>
- Simon, S., Bößwetter, A., Bagdonat, T., Motschmann, U., & Glassmeier, K.-H. (2006). Plasma environment of Titan: A 3-d hybrid simulation study. *Annales Geophysicae*, *24*(3), 1113–1135. <https://doi.org/10.5194/angeo-24-1113-2006>
- Smith, H. T., Mitchell, D. G., Johnson, R. E., Mauk, B. H., & Smith, J. E. (2019). Europa neutral torus confirmation and characterization based on observations and modeling. *Acta Pathologica Japonica*, *87*(1), 69. <https://doi.org/10.3847/1538-4357/aaed38>
- Squyres, S. W., Reynolds, R. T., & Cassen, P. M., Peale, S. J. (1983). Liquid water and active resurfacing on Europa. *Nature*, *301*(5897), 225–226. <https://doi.org/10.1038/301225a0>
- Strazzulla, G., Baratta, G. A., Leto, G., & Gomis, O. (2007). Hydrate sulfuric acid after sulfur implantation in water ice. *Icarus*, *192*(2), 623–628. <https://doi.org/10.1016/j.icarus.2007.08.004>
- Vasyliunas, V. M. (1983). Plasma distribution and flow. In *Physics of the Jovian magnetosphere* (pp. 395–453). Cambridge University Press. <https://doi.org/10.1017/cbo9780511564574.013>
- Vay, J.-L. (2008). Simulation of beams or plasmas crossing at relativistic velocity. *Physics of Plasmas*, *15*(5), 056701. <https://doi.org/10.1063/1.2837054>
- Volwerk, M., Khurana, K., & Kivelson, M. (2007). Europa's Alfvén wing: Shrinkage and displacement influenced by an induced magnetic field. *Annales Geophysicae*, *25*, 905, 914. <https://doi.org/10.5194/angeo-25-905-2007>
- Volwerk, M., Kivelson, M. G., & Khurana, K. K. (2001). Wave activity in Europa's wake: Implications for ion pickup. *Journal of Geophysical Research*, *106*(A11), 26033–26048. <https://doi.org/10.1029/2000JA000347>
- Vorburger, A., & Wurz, P. (2018). Europa's ice-related atmosphere: The sputter contribution. *Icarus*, *311*, 135–145. <https://doi.org/10.1016/j.icarus.2018.03.022>
- Zimmer, C., Khurana, K. K., & Kivelson, M. G. (2000). Subsurface oceans on Europa and Callisto: Constraints from Galileo magnetometer observations. *Icarus*, *147*(2), 329–347. <https://doi.org/10.1006/icar.2000.64562145>